



Physical and biogeochemical impacts of RCP8.5 scenario in the Peru upwelling system

Vincent Echevin¹, Manon Gévaudan^{1,2,3}, Dante Espinoza-Morriberon², Jorge Tam², Olivier Aumont¹,
5 Dimitri Gutierrez^{2,4}, François Colas^{1,2}

¹Sorbonne Université, LOCEAN-IPSL, CNRS/IRD/MNHN, 4 place Jussieu, 75252 Paris, France

²Instituto del Mar del Peru (IMARPE), Esquina General Gamarra y Valle, Callao, Perú

³Laboratoire d'Etudes en Géophysique et Océanographie Spatiales, 14 av. E.Belin, 31400 Toulouse, France

10 ⁴Laboratorio de Ciencias del Mar, Universidad Peruana Cayetano Heredia, Lima, Perú

Correspondence to: Vincent Echevin (vincent.echevin@ird.fr)

Abstract:

15 The northern Humboldt current system (NHCS or Peru upwelling system) sustains the world's largest small pelagic fishery. While a nearshore surface cooling has been observed off southern Peru in recent decades, there is still considerable debate on the impact of climate change on the regional ecosystem. This calls for more accurate regional climate projections of the 21st century, using adapted tools such as regional eddy-resolving coupled biophysical models. In this study 3 coarse-grid Earth System Models (ESMs) from the Coupled Model Intercomparison Project (CMIP5) are selected based on their
20 biogeochemical biases upstream of the NHCS and simulations for the so-called business-as-usual RCP8.5 climate scenario are dynamically downscaled at 10 km resolution in the NHCS. The impact of regional climate change on temperature, coastal upwelling, nutrient content, deoxygenation and the planktonic ecosystem is documented. We find that the downscaling approach allows to correct major physical and biogeochemical biases of the ESMs. All regional simulations display a surface warming regardless of the coastal upwelling trends. Contrasted evolutions of the NHCS oxygen minimum zone and enhanced
25 stratification of phytoplankton are found in the coastal region. Whereas trends of downscaled physical parameters are consistent with ESM trends, downscaled biogeochemical trends differ markedly. These results suggest that more realism of the ESMs is needed in the eastern equatorial Pacific to gain robustness in the projection of regional trends in the NHCS.

1 Introduction

30 Eastern Boundary Upwelling Systems (EBUS) are oceanic systems where alongshore winds generate the upwelling of deep, cold and nutrient-replete waters. This drives a high biological productivity and thriving small pelagic fish fisheries which are major sources of income for the adjacent countries. In particular, the Peruvian Upwelling System (also known as the Northern Humboldt Current System, NHCS in the following), located in the South Eastern Tropical Pacific, is the most



productive EBUS in terms of fish catch (Chavez et al., 2008), due to its rich anchovy fishery. Moreover, the subsurface water masses in the NHCS are located in the poorly ventilated so-called “shadow zone” of the south eastern Pacific (Luyten et al., 1983). This low ventilation creates a subsurface water body with very low oxygen concentration, the oxygen minimum zone (OMZ). The OMZ results from a balance between oxygen consumption by respiration of large amounts of organic matter exported from the highly productive surface layer, and ventilation by the equatorial current system composed of eastward jets transporting relatively oxygenated waters (Czeschel et al., 2011; Montes et al., 2014). A particular aspect of the NHCS OMZ is its very low oxygen concentration (anoxia) at relatively shallow depths, which impacts the local marine ecosystem (Stramma et al., 2010; Bertrand et al., 2011).

In the recent decades, public concern has risen about the impact of climate change on EBUS. Using ship wind observations, Bakun (1990) showed that upwelling-favorable winds increased over recent decades (1950-1990) in several EBUS. He proposed that nearshore winds would continue to intensify due to an enhanced differential heating between land and sea, driven by a stronger greenhouse effect over land. However, this hypothesis has been challenged in the NHCS because of observation bias (e.g. Tokinaga and Xie, 2011) and poleward displacement of the South Pacific Anticyclone (Belmadani et al., 2013; Rykaczewski et al., 2015). Nevertheless, in situ and satellite Sea Surface Temperatures (SST) show a conspicuous surface coastal cooling off southern Peru (15°S) since the 1950s. This cooling, consistent with a wind increase found in ERA40 reanalysis, suggests a possible intensification of the wind-driven upwelling (Gutierrez et al., 2011).

Recent analysis of IPCC global circulation models (GCMs) reported that the intensification of nearshore winds under scenarios of carbone dioxide concentration increase is mainly confined to the poleward portions of EBUS (Wang et al., 2015; Rykaczewski et al., 2015, Öyarzun and Brierley, 2019). However, the evolution of winds in the NHCS remains unclear (note that the entire NHCS *stricto sensu* was not included in these studies). Furthermore, the realism of IPCC GCMs is hampered by the coarse resolution of the model grids (~100-200 km), that does not allow to represent the details of coastal orography and coastline that influence the coastal wind structure.

A few downscaling studies focusing on regional wind changes in the NHCS have provided invaluable information. NHCS upwelling-favorable winds may weaken in the future, mainly during the productive austral summer season (Goubanova et al., 2011; Belmadani et al., 2014). However, only idealized extreme scenarios (AR4 preindustrial, doubling (2xCO₂) and quadrupling (4xCO₂) of carbon dioxide concentration) from a single GCM (IPSL-CM4, Marti et al., 2010) were downscaled in these studies. In line with these studies, Echevin et al. (2011) used a regional ocean circulation model (RCM) forced by statistically downscaled atmospheric winds from Goubanova et al. (2011) to downscale the NHCS ocean temperature and circulation changes under 2xCO₂ and 4xCO₂ scenarios. They found a strong warming in the surface layer, of up to ~+5°C nearshore in the 4xCO₂ scenario with respect to preindustrial conditions, and an upwelling decrease during austral summer. Following the same regional modeling approach and using the downscaled winds from Belmadani et al. (2014), Oerder et al. (2015) found a year-round reduction in upwelling intensity, mitigated by an onshore geostrophic flow. The shoaling of upwelling source waters in the 2 scenarios suggests that upwelled waters could become less nutrient-rich, and thereby reduce nearshore primary productivity (Brochier et al., 2013).

The impact of climate change on the NHCS productivity, oxygenation and acidification has been even less investigated. Assuming Bakun's (1990) hypothesis of increasing coastal winds, Mogollón and Calil (2018) found a moderate



70 increase (5%) of the NHCS productivity using a RCM. However, they did not take into account the large-scale stratification
changes driven by climate change that may significantly contribute to nearshore stratification and mitigate the upwelling
(Echevin et al. 2011, Oerder et al., 2015). Following a similar approach, Franco et al.(2018) found a sustained acidification of
NHCS shelf and slope waters under the Representative Concentration Pathway 8.5 scenario (RCP8.5, the most pessimistic
AR5 climate scenario corresponding to a 8.5 Wm^{-2} heat flux driven by the greenhouse effect, e.g. van Vuuren et al., 2011),
75 driven by changes in surface fluxes of atmospheric CO_2 concentration and subsurface dissolved inorganic carbon
concentrations. However, as in Mogollón and Calil (2017), the impact of climate change on NHCS surface winds, circulation
and stratification was unaccounted for in Franco et al. (2018).

In brief, previous regional modelling experiments were either obtained from (i) the downscaling of one single GCM or
Earth System Model (a GCM including a biogeochemical model, hereafter ESM), (ii) the analysis of relatively short time
80 periods (e.g 30 years in the stabilized phase of the $2\times\text{CO}_2$ and $4\times\text{CO}_2$ scenarios in Echevin et al., 2011; Oerder et al.,2015;
Brochier et al.,2013), or (iii) simplified approaches that did not account for all physical forcings (e.g. Mogollón and Calil,
2018; Franco et al., 2018). More work is thus needed to evaluate the robustness of these findings in the context of more recent
climate scenarios (e.g. RCP8.5).

In the present work, 3 different ESMs are dynamically downscaled in the NHCS using a regional coupled dynamical-
85 biogeochemical model. The time period of study is 2005-2100 under the RCP8.5 scenario. The regional trends from RCMs
are compared to illustrate the diversity of climate change regional impacts. RCM trends are also contrasted with those of the
ESMs in order to highlight the impact of the downscaling process. In the following paragraphs, we choose to study the trends
of key physical and biogeochemical parameters, such as temperature, coastal upwelling, thermocline depth, oxygenation,
nitrate and productivity. In the next section (section 2), the choice of ESMs and downscaling methodology are described.
90 Results are presented in section 3 and discussed in section 4. Conclusions are drawn in section 5.

2 Methodology

2.1 Ocean model

The Regional Ocean Modeling System (ROMS) was used to simulate the ocean dynamics. The ROMS_AGRIF (version
95 v3.1.1 is used in this study) resolves the Primitive Equations, which are based on the Boussinesq approximation and
hydrostatic vertical momentum balance (Penven et al., 2006; Shchepetkin and McWilliams, 2009). A fourth-order centered
advection scheme allows the generation of steep tracer and velocity gradients (Shchepetkin and McWilliams, 1998). For a
complete description of the model numerical schemes, the reader can refer to Shchepetkin and McWilliams (2005).

The model domain spans over the coasts of south Ecuador and Peru from 5°N to 22°S and from 95°W to 69°W . It is close to
100 the one used in Penven et al. (2005). The horizontal resolution is $1/9^\circ$, corresponding to $\sim 12 \text{ km}$. The bottom topography
from ETOPO2 (Smith and Sandwell, 1997) is interpolated on the grid and smoothed in order to reduce potential errors in the
horizontal pressure gradient. The vertical grid has 32 sigma levels.

Wind speed, air temperature and humidity, and ROMS SST are used to compute latent and sensible heat flux online using a
bulk parameterization (Liu et al., 1979).



2.2 Biogeochemical model

ROMS is coupled to the Pelagic Interaction Scheme for Carbon and Ecosystem Studies (PISCES) biogeochemical model. PISCES simulates the marine biological productivity and the biogeochemical cycles of carbon and main nutrients (P, N, Si, Fe; Aumont et al., 2015) as well as dissolved oxygen (DO) (e.g., Resplandy et al., 2012, Espinoza-Morriberón et al., 2019). It has three non-living compartments which are the semi-labile dissolved organic matter, small sinking particles and large sinking particles, and four living compartments represented by two size classes of phytoplankton (nanophytoplankton and diatoms) and two size classes of zooplankton (microzooplankton and mesozooplankton). The ROMS-PISCES coupled model has been used to study the climatological (Echevin et al., 2008), intraseasonal (Echevin et al., 2014), and interannual variability of the surface productivity (Espinoza-Morriberón et al., 2017) and oxygenation (Espinoza-Morriberón et al., 2019) in the NHCS. Details of the parameterizations can be found in Aumont et al. (2015). However we need to stress some differences in the PISCES version used in this study: i) diatoms and nanophytoplankton growth, microzooplankton grazing and mortality, mesozooplankton mortality depend on temperature (T) and are proportional to $\exp(a.T)$ with $a=0.064 \text{ } ^\circ\text{C}^{-1}$; ii) mesozooplankton grazing on nanophytoplankton and diatoms is proportional to $\exp(b.T)$ with $b=0.076 \text{ } ^\circ\text{C}^{-1}$. These differences, in particular the larger temperature-enhanced mesozooplankton grazing with respect to phytoplankton growth, can play an important role in the context of surface warming in the NHCS. Boyd et al. (1981) measured grazing of Peruvian copepods, however further laboratory experiments are needed at different temperatures to calibrate these rates.

2.3 Selection of the Earth System Models

3 CMIP5 ESMs are selected for the regional downscaling. The selection process is based on the nutrients simulated by the ESMs and on the evaluation of biogeochemical bias (the temperature and salinity biases are weak in comparison with biogeochemical bias, Figures not shown). Only 5 ESMs (CNRM, GFDL, IPSL, CESM and Nor-ESM) represent the four nutrients (silicate, phosphate, nitrate and iron) and oxygen required by PISCES. As different ESM versions were available, a total of 8 ESMs (CNRM-CM5, GFDL-ESM2M, GFDL-ESM2G, IPSL-CM5A-MR, IPSL-CM5A-LR, IPSL-CM5B-LR, CESM1, Nor-ESM1-ME) were compared to observations from the World Ocean Atlas (WOA2009, Fig.1). Following Cabré et al. (2015), the ESM variables were averaged at 100°W between 5°N and 10°S , near the location of the western open boundary of the model. This meridional section intersects eastward jets: the Equatorial Undercurrent (EUC) at 0°S and the off-equatorial subsurface countercurrents (SSCCs) at $\sim 4^\circ\text{S}$ and $\sim 8^\circ\text{S}$ (Montes et al., 2010). These jets transport physical and biogeochemical properties to the Peru upwelling region (Montes et al., 2010, 2014; Oerder et al., 2015; Espinoza-Morriberon et al., 2017, 2019).

All ESMs simulate an oxygen decrease with depth (Fig.1a), but oxygen values are too low (i.e. $<10 \mu\text{mol l}^{-1}$) in CESM1-BGC, GFDL-ESM2M, GFDL-ESM2G and NorESM1-ME. Slightly negative values are attained below 300 m depth for GFDL-ESM2G. CNRM-CM5. In contrast, the 3 IPSL model versions, which all include PISCES as biogeochemical component, overestimate the oxygen content above ~ 600 m depth. Note that only CESM1-BGC is able to reproduce the observed oxygen increase below 400 m depth, which corresponds to the lower limit of the OMZ.

In terms of nitrate concentration, the most realistic models in the upper 300 meters are GFDL-ESM2G, GFDL-ESM2M and CESM1-BGC (Fig.1b). However the model biases become negative and increase strongly at depths greater than



300 m. A negative bias found in the 3 IPSL ESMs ($\sim 3\text{--}4 \mu\text{mol l}^{-1}$ for IPSL-CM5A-MR and IPSL-CM5A-LR and $\sim 6\text{--}8 \mu\text{mol l}^{-1}$ for IPSL-CM5B-LR) is roughly constant over depth. CESM1-BGC, GFDL-ESM2G and NorESM1-ME display too low nitrate concentrations below 250 m depth, possibly due to denitrification in the anoxic OMZ (Fig.1a).

145 The GFDL-ESM2M phosphate profile is very close to the observations (Fig.1c), whereas the 3 IPSL ESMs and CNRM-CM5 underestimate phosphate concentrations with a roughly constant bias over depth (negative bias of $\sim 0.5\text{--}1 \mu\text{mol l}^{-1}$). In contrast, NorESM1-ME, GFDL-ESM2G and CESM1-BGC overestimate the phosphate concentrations.

150 The IPSL ESMs silicate profiles and CESM1-BGC are close to observations above ~ 250 m depth, whereas the positive bias in GFDL-ESM2M and NorESM1-ME increases below 200 m depth. The CNRM-CM5 negative bias is moderate between 50 and 300 m depth (Fig.1d).

To conclude, as the 3 IPSL ESMs and CNRM-CM5 include the PISCES model and provide relatively realistic results in terms of nutrient profiles, IPSL-CM5A-MR (deemed slightly more realistic than the 2 others) and CNRM-CM5 are selected. We also select GFDL-ESM2M, which represents well the nitrate and phosphate profiles in the upper layers, and whose bias did not increase at depth as in GFDL-ESM2G. CESM1-BGC also performs quite well, but some variables were 155 not available from the archive (e.g. 10 m wind) at the beginning of this study. We thus restricted our study to 3 ESMs.

The main characteristics of the selected ESM ocean models (grid spacing and biogeochemical structure) are summarized in table 1. We refer to the ESMs as CNRM, IPSL and GFDL in the following sections and figures.

2.4 Atmospheric forcing methodology:

160 A bias correction is used to construct forcing files (e.g. Oerder et al., 2015). For each forcing variable X (i.e. X =wind velocity, air temperature, ...), the bias-corrected variable X' is computed as follows:

$$X' = X_{\text{OBSclim}} + (X_{\text{ESM-RCP8.5}} - X_{\text{ESM-hist-clim}}) \quad (1)$$

X_{OBSclim} corresponds to a monthly climatology of observed values, $X_{\text{ESM-RCP8.5}}$ corresponds to the coarse-grid ESM values for each month, and $X_{\text{ESM-hist-clim}}$ to a monthly climatology of the coarse-grid ESM values during the historical period (2000-2100).

165 This allows subtracting the ESM mean bias, assuming that it remains identical over the historical period and over 2000-2100. This method has been used in several papers (Cambon et al. 2013; Echevin et al. 2013; Oerder et al., 2015). The SCOW (Risien and Chelton, 2008) surface wind and COADS (Da Silva et al., 1994) downward shortwave and longwave fluxes and air parameters (temperature and specific humidity) climatologies were used for X_{OBSclim} .

170 2.5 Open boundary and initial conditions for physics and for biogeochemistry

As in Echevin et al. (2010) and Oerder et al. (2015), the ESM monthly sea level, temperature, salinity, horizontal velocity at the locations of the RCM open boundaries are directly interpolated on the model grid without bias correction. Given the important bias of the ESM mean biogeochemical state (e.g. Bopp et al., 2013; Cabré et al., 2015), we apply the bias correction described in Eq.(1): we add the WOA2009 ($1^\circ \times 1^\circ$) monthly climatology of the biogeochemical variables (nitrate, 175 silicate, phosphate, iron, DIC, DOC, alkalinity) and the annual mean anomalies (see Eq.(1)). Note that we do not use the ESM oxygen variability due to the strong oxygenation trend found at 95°W in the CNRM (see Fig.17 and section 4.3). In order to keep the same forcing methodology for all RCMs, WOA2009 monthly OBCs are used for oxygen. Oxygen



180 variability in the RCMs is thus only driven by the physical variability and potentially by biogeochemical processes impacting the oxygen cycle, and not by the variability of oxygen concentration at the open boundaries of the regional domain. The 3D fields were interpolated on the ROMS grid using the ROMSTOOLS package (Penven et al., 2008).

The three simulations are initialized as follows. Initial conditions from the ESM physical parameters of the historical simulation (2000-2010 January average) and WOA biogeochemical values (January) constitute the initial state. A 9-year spin up simulation from 1997 to 2005 is then performed to reach equilibrium. The runs are then forced by RCP8.5 conditions until 2100. State variables and biogeochemical rates (e.g. primary production) are stored every 5 days. The regional simulations 185 are named R-IPSL, R-CNRM, R-GFDL in the following.

2.6 Additional data sets

Two ocean reanalysis products are used to evaluate the ESM equatorial circulation and thermocline in present conditions. The SODA 2.3.4 Reanalysis (Carton and Giese, 2008) over the period 1992–2000 assimilates observational data 190 in a general circulation model with an average horizontal resolution of 0.25°. The recently available GLORYS12V1 Reanalysis over the period 1993-2017 is also used (Ferry et al., 2012). Altimeter data, in situ temperature and salinity vertical profiles and satellite SST were jointly assimilated in GLORYS12V1 (Lellouche et al., 2018). This product is freely distributed by the Copernicus Marine Environment Monitoring Service.

Several sets of observations are used to evaluate the realism of ESMs and RCMs in present conditions (i.e. 2006-2020 195 period). In situ data include CARS2009 gridded (0.5°x0.5°, Rigway et al., 2002) fields of nitrate and oxygen, high resolution (0.1°x0.1°) regional monthly climatologies of temperature (Grados et al., 2018) and oxygen (Graco et al., 2018) including measurements collected during IMARPE (The Sea Institute of Peru) cruises. AVHRR satellite SST (2006-2015) is used to assess the RCM SST. Surface chlorophyll-a monthly climatologies from SeaWiFS (1997-2010) and MODIS (2002-2015) are used to evaluate the RCM surface chlorophyll.

200

2.8 Coastal indices

Time series of coastal indices characterizing the variability over the central Peru shelf for specific variables are computed. The variables are averaged in a coastal band extending from the coastline to 100 km offshore and between 7°S and 13°S.

205 An index of coastal upwelling, the cross-shore transport in a coastal band, is computed from the model output, following Colas et al. (2008) and Oerder et al. (2015). The mean horizontal transport is computed each month in a coastal strip extending from 7°S to 13°S and from the coast to 100 km offshore. The transport is integrated over the Ekman layer depth. This index, in contrast with upwelling indices based on alongshore wind stress values only, takes into account the potential role of the cross-shore geostrophic current which can modulate the coastal upwelling (e.g. during El Niño events, 210 Colas et al. (2008), Espinoza-Morriberon et al., 2017). The method is detailed in Oerder et al. (2015).

2.9 Statistical methods

Only time scales longer than 5 years are studied in this work. Therefore the time series are low-pass filtered using a



215 ten-year moving average. This allows to filter the ENSO variability which is very strong in the NHCS, but not the focus of
the present study. Linear trends of the time series are computed using a least squares method. The percentage of change
between 2006 and 2100 associated with the linear trends are indicated on the right side of the figures and listed in 3 Tables :
Table 2 for physical variables, Table 3 for oxygen and nitrate, and Table 4 for chlorophyll and zooplankton.

3 Results

220 In the following sections we show that the RCM is able to represent the main characteristics of the NHCS coastal
upwelling system thanks to its high spatial resolution (relatively to the ESMs). We then describe the long-term trends over the
period 2006-2100 under the RCP8.5 scenario for key downscaled physical (surface and subsurface temperature, heat and
momentum fluxes, upwelling) and biogeochemical parameters (oxygen and nutrient content, primary productivity, planktonic
225 biomass) in the upwelling system but also in the equatorial band offshore of the NHCS. For selected variables we also
compare the downscaled simulations and the coarse-grid ESMs. In the next section, we first characterize the downscaled
physical fields.

3.1 Physical variability

230 Sea Surface Temperature spatial patterns

We first contrast the Sea Surface Temperature (SST) patterns of the ESMs and RCMs to highlight the efficiency of the
dynamical downscaling. The actual observed SST displays the cool water tongue along the coast and associated cross-shore
SST gradient, characteristic of coastal upwelling (Fig.2a). The RCM simulates correctly the upwelling features (Fig.2b). The
fine representation of the coastline, shelf and slope topography and debiased alongshore winds (see section 2.4) all play a role
235 in the correct representation of the upwelling structure. In contrast, The ESM SST (CNRM is shown here as an example,
similar results are found for IPSL and GFDL) in present conditions (2006-2015) displays a warm bias of 2-4°C typical of
ESMs (Flato et al., 2013) and no clear sign of coastal upwelling (Fig.2c). In 2091-2100, the RCM displays a coastal
upwelling of waters ~2-3°C warmer than in 2006-2015 (Fig.2d). Again the ESM SST spatial pattern in 2091-2100 (Fig.2e)
resembles that of 2006-2015. Coastal upwelling is not present and a warming of ~2-3 °C is found over the main part of the
240 domain.

Trends of nearshore SST

A steady warming of the surface coastal ocean is found in the three regional simulations (Fig 3a). SST increases
rapidly in R-IPSL since the 2020s, reaching +4.5°C in 2100, whereas it increases since the 2030s in the other simulations,
245 reaching +3.5°C and +2°C in R-CNRM and R-GFDL respectively. Interestingly, decadal variability can produce decades
during which the SST increase is stalled (or so-called “hiatus”), e.g. in 2035-2045 in R-CNRM and in 2040-2060 in R-GFDL.
The ESM linear trends are very similar to the RCM nearshore warming trends (Fig.3b, Table 2). The offset between the 3
ESM SST evolutions is due to the different SST bias in 2005 (between 4-6°C among the ESMs, Fig.3b). These warming
trends contrast with the greenhouse gas-driven cooling in EBUS projected by Bakun (1990) and Bakun et al. (2010). As an



250 example, the spatial structures of the CNRM RCM and ESM SST anomalies are compared (Figs.3c,d). The similarity
between the two anomaly patterns is striking. Both display a maximum warming near the coasts and west of the Galapagos
where upwelling occurs. This indicates that subsurface positive anomalies upwelled to the surface are partly damped as they
are transported offshore by the surface currents.

255 **Temporal variability of heat and momentum fluxes**

As expected from greenhouse effect, downward longwave radiation increases steadily over the 21st century in all
ESMs under RCP8.5 (Fig.4a). The increase is stronger in IPSL (+10%, see Table 2) and CNRM (10%) than in GFDL (7%).
Contrasted downward shortwave radiation trends are simulated by the ESMs (Fig.4b). Insolation decreases quasi-linearly in
CNRM (-7%) and in GFDL (-4%), however it is strongly modulated by decadal variability in GFDL (note the slight
260 insolation increase in 2090-2100). On the other hand, IPSL displays no trend (0%). Alongshore wind stress, the main driver
of coastal upwelling, decreases in CNRM (-11%) and IPSL (-9%) in contrast with GFDL (+2%) (Fig 4c). The wind decrease
in IPSL and CNRM is consistent with that found in CMIP3 simulations (Goubanova et al.2010; Belmadani et al. 2013).

Coastal upwelling

265 The net offshore flux, a proxy of coastal upwelling, decreases strongly in R-IPSL (-23%) and R-CNRM (-25%) (Fig.5a,
Table 2). These downward trends are consistent with the wind stress trends (Fig.4c) but more than twice larger. In contrast,
coastal upwelling remains stable in R-GFDL. The net offshore flux is strongly modulated by decadal variability, whose
amplitude can reach 5-10% of the mean value. Decadal variability may generate decades of upwelling increase (e.g. in 2090-
2100 in R-CNRM) masking the long term decrease. Upwelling decadal variability is mainly forced by variations of the
270 onshore geostrophic transport, which on average mitigates ~50% of the wind-driven upwelling (Fig.5b). This onshore current
is driven by the higher sea level in the equatorial portion of the upwelling system than in its poleward portion (Colas *et al.*
2008; Oerder *et al.*, 2015). It is occasionally remarkably strong (e.g. in 2090 in R-CNRM, 2035-2040 and 2065 in R-GFDL).

Subsurface temperature anomalies

275 Nearshore subsurface temperature anomalies are mainly related to equatorial subsurface temperature anomalies which
propagate along the equatorial and coastal wave guide (e.g. Echevin *et al.*, 2011, 2014; Espinoza *et al.*, 2017, 2018).
Subsurface temperature anomalies are also transported eastward and poleward by the near-equatorial subsurface jets (Fig.2a;
Montes *et al.*, 2010, 2011). The thermocline is strongly impacted by climate change in the eastern equatorial Pacific. The
depth of the 20°C isotherm (hereafter D20) increases in all ESMs, at different rates (Fig.6a). The deepening is roughly linear
280 in GFDL (+5%, Table 2) and CNRM (+26%). In contrast, it increases non-linearly in IPSL, first by ~1.5 m/decade between
2005 and 2065, and then by ~5 m/decade between 2065 and 2100. Note that D20 is shallower in the ESMs (~30-40 m) than
in observations (~52 m in WOA) and in two ocean reanalysis (~56 m in GLORYS2V1 and -58 m in SODA). A shallow
thermocline is likely to be more impacted by greenhouse-induced surface warming in the model simulations than in the real
ocean.

285 D20 coastal trends in the RCMs (Fig.6b) are roughly similar to the offshore ESM equatorial trends. The coastal



deepening is moderate in R-GFDL (+12%, Table 2). In contrast, a strong linear deepening is found in R-CNRM (+101%). As in the equatorial region, D20 deepening is non linear in R-IPSL and the thickness of the surface layer more than doubles (+207%). The RCM D20 values at the beginning of the century are within the range of estimated values from observations and reanalyses whereas D20 is too deep in the ESMs, which highlights the dynamical downscaling ability to reduce part of this systematic bias. The RCM trends are roughly in line with the ESM coastal trends. D20 deepening can be exacerbated (e.g. 207% in R-IPSL vs 126% in IPSL) or mitigated (12% in R-GFDL vs ~21% in GFDL, Fig.6c) depending on the model. Decadal variability from the equatorial region propagates to the coastal regions with little change.

A shoaling of the mixed layer is found in all simulations (Fig.7), in line with the surface heating (Fig.4a,b) and reduced wind-driven mixing (Fig.4c). The shoaling is slightly stronger in R-IPSL and R-GFDL than in R-CNRM, possibly due to the stronger surface warming in R-IPSL (Table 2). The R-GFDL mixed layer depth in 2006-2015 is in good agreement with the climatological value from the low-resolution 2°x2° gridded product of de Boyer Montégut et al.(2004), whereas R-IPSL and R-CNRM are ~ 3 m shallower. Note that the methods for calculating mixed layer depth in de Boyer Montégut et al. (2004) and in the ocean model are different.

The near-equatorial subsurface, coastal subsurface and surface temperature linear trends of the 3 RCMs are compared in Figure 8. Near-equatorial subsurface trends are weakest in R-GFDL and strongest in R-IPSL, which is consistent with the D20 deepening (Fig.6a). A similar ranking from weakest (R-GFDL) to strongest warming (R-IPSL) is found for the coastal subsurface warming and coastal surface warming. The equatorial water masses are transported towards the coasts (Montes et al., 2010; Oerder et al., 2015) and the subsurface layer trends increase by 6% in R-GFDL, 23% in R-CNRM and 10% in R-IPSL with respect to the near-equatorial trends. Furthermore the coastal SST trends increase with respect to the coastal subsurface anomalies (+17% in R-GFDL, +37% in R-CNRM, +44% in R-IPSL), highlighting the impact of different local heat fluxes. In the coastal region, the upper part of the 50-200m subsurface water volume is upwelled into the mixed layer where additional heat is deposited by the local atmospheric fluxes (Figs. 4a,b). In conclusion, RCM coastal subsurface and surface trends can not be derived linearly from the ESM equatorial temperature trends.

310

3.2 Biogeochemical response of the NHCS under RCP8.5 scenario

We now investigate the impacts of regional climate change on the main biogeochemical characteristics of the NHCS, namely oxygenation, nutrients and productivity.

315 OMZ trends in response to the equatorial circulation

The weak subsurface dissolved oxygen (DO) concentrations found in the NHCS result from a subtle balance between the eastward and poleward transport of relatively oxygenated waters from the equatorial region into the upwelling region, ventilation due to mesoscale circulation (Thomsen et al., 2016; Espinoza et al., 2019) and local DO consumption due to the respiration of sinking organic matter. The eastward currents in the offshore equatorial region thus play an important role in the ventilation of the OMZ (Stramma et al., 2008; Montes et al., 2014; Cabré et al., 2015; Shigemistu et al., 2017; Espinoza-Morriberon et al., 2019). Following Cabré et al. (2015) we first evaluate the ESM eastward subsurface flow at 95°W (Fig.9a).

320



As estimates of mean velocity from ocean reanalysis range between 0.05 m s^{-1} (GLORYS12V1) and 0.09 m s^{-1} (SODA), the uncertainty of the eastward flow is very high. The eastward flow in R-GFDL (in 2005-2010) is $\sim 10\%$ weaker than in SODA. In contrast, the eastward flow is underestimated by $\sim 50\%$ in R-CNRM and R-IPSL with respect to SODA, probably because
325 of a weak EUC and/or weak SSCCs in these coarse-grid ESMs (Cabr e et al., 2015). Over 2006-2100, the eastward velocity is stable ($<1\%$, Fig.9a, Table 2) in R-CNRM, decreases weakly in R-IPSL (-9%) and in R-GFDL (-14%).

As fixed DO OBCs are used in our simulations, the evolution of the eastward DO flux at 95°W (Fig.9b) follows approximately that of the mass flux. It is relatively weak in R-CNRM (-2% , Table 3) and decreases more strongly in the other two simulations (-7% in R-IPSL and -10% in R-GFDL). Note that the DO eastward flux is $\sim 25\text{-}30\%$ stronger in R-IPSL
330 than in R-CNRM, due to a stronger (weaker) eastward flow between 2°S and 10°S (2°S and 2°N) in R-IPSL than in R-CNRM (Figure not shown). As the water is more oxygenated south of the $2^\circ\text{S}\text{-}2^\circ\text{N}$ equatorial band (e.g. Figure 4 in Cabr e et al., 2015), this results in a stronger oxygen flux in R-IPSL than in R-CNRM.

The evolution of the NHCS nearshore DO concentration (i.e the DO concentration in the upper part of the OMZ between 100 and 200m, Fig.10a) indicates that the DO content in 2006-2015 is higher in R-GFDL ($\sim +10 \mu\text{mol L}^{-1}$) than in the observations ($\sim 15\text{-}18 \mu\text{mol L}^{-1}$) and lower in R-IPSL and R-CNRM ($\sim -5 \mu\text{mol L}^{-1}$). The eastward flux at 95°W brings DO
335 to the OMZ in greater proportions in R-GFDL than in R-IPSL and R-CNRM (Fig.9b), partly explaining these discrepancies. However, differences in production and export of organic matter in the simulations also affect the DO content. This aspect will be discussed in section 4.3. The nearshore trends are very different among the three simulations. The DO content decreases rapidly in R-GFDL (-38% , Table 3) and more slowly (-10%) in R-IPSL, whereas it increases strongly in R-CNRM
340 ($+36\%$). R-GFDL is also marked by a much stronger multidecadal variation than the the other RCMs.

The depth of the 0.5 mL L^{-1} ($22 \mu\text{mol L}^{-1}$) DO iso-surface (hereafter named “oxycline”) is often used as a proxy for the OMZ upper limit (e.g. Espinoza-Morriberon et al., 2019) which characterizes the vertical extent of the habitat of many living species in this coastal ecosystem. The oxycline in R-IPSL and R-CNRM are $\sim 10\text{-}30 \text{ m}$ shallower than the observed oxycline in the IMARPE climatology. The latter is $\sim 35 \text{ m}$ shallower and likely more realistic than the WOA oxycline depth
345 because to its high resolution (10 km) which allows to represent the oxycline shoaling towards the coast (not shown). Oxycline variations (Fig.10b) are expectedly anticorrelated with the variations of the subsurface DO content. The oxycline shoals rapidly in R-GFDL, weakly in R-IPSL whereas it slightly deepens in R-CNRM. Similar trends are found for the “upper oxycline” defined by the 1 mL L^{-1} isoline (not shown, see Table 3).

350 Nitrate trends

As ESM mean nitrate concentrations in the equatorial region are deemed realistic enough (Fig.1b), their temporal variations over 2006-2100 are taken into account at the RCM OBCs. A decrease of subsurface nitrate concentrations at 95°W is found in all simulations (Fig. 11a), varying between strong (-18% in R-CNRM) and weak depletion (-7% in R-IPSL and -5% in R-GFDL, Table 3). Nitrate depletion was also found in IPSL CMIP3 $4\times\text{CO}_2$ scenario (Brochier et al., 2013). It is
355 likely caused by a reduced nutrient delivery from the deep ocean to the upper layers of the ocean associated to enhanced thermal stratification, reduced vertical mixing and overall slowdown of the ocean circulation (e.g. Fr licher et al, 2010). Due to the stronger eastward flow in R-GFDL (Fig.9a), the associated nitrate eastward flux is $\sim 50\%$ stronger than in R-IPSL and



R-CNRM (Fig. 11b). The fluxes decrease in all simulations (-27% in R-CNRM, -20% in R-IPSL, -18% in R-GFDL, Table 3, Fig. 11b). Following Espinoza-Morriberon et al. (2017), the depth of the $21 \mu\text{mol L}^{-1}$ nitrate iso-surface in the coastal region is chosen as a proxy of the nitracline depth (Fig. 11c). In spite of the decreasing nitrate flux (-18%, Fig. 11b) from the offshore near-equatorial eastern boundary, the nearshore nitracline shoals in R-GFDL (-25%). In contrast, it deepens in R-IPSL (+37%) and in R-CNRM (~+150%). This shows that the equatorial forcing is not always the main forcing of the evolution of the nearshore nitracline depth: whereas it seems to drive nitrate depletion in R-CNRM and R-IPSL, the maintained coastal upwelling in R-GFDL (Fig. 5a) could play a role in the compensation of this effect. It is also notable that the nitracline may shoal even though coastal upwelling does not increase (e.g. in R-GFDL, Fig. 5a). This points to potential changes in nitrate vertical distribution, possibly due to a reduction of nitrate assimilation driven by biomass variations (see section 3.3). The ESM nearshore nitracline trends are roughly consistent with the RCMs, but the values are different: nitracline deepening is more moderate in CNRM (~100%, Table 3) than in R-CNRM (~150%), and nitracline shoaling in R-GFDL (-25%) is quasi absent in GFDL (+2%). Note that the nitracline (i.e. depth of $21 \mu\text{mol L}^{-1}$) is too shallow in RCMs (~20-35 m over 2006-2015 vs ~100 m in CARS) due to an overly high nitrate concentration in subsurface layers (figure not shown). This bias was also found in previous ROMS-PISCES regional simulations of the NHCS (e.g. see also Fig. 3 in Espinoza-Morriberon et al., 2017) possibly due to lack of denitrification.

Chlorophyll and primary productivity annual variations

Regional downscaling has a strong impact on the nearshore planktonic biomass. Chlorophyll is used in the following as a proxy of total phytoplankton biomass. The annual-mean surface chlorophyll concentration in 2006-2010 (Fig. 12a) agrees relatively well with MODIS mean chlorophyll (~4.25 mg Chl m^{-3}) in R-IPSL (~4.2 mg Chl m^{-3}) and R-GFDL (~4.5 mg Chl m^{-3}) and is ~30% higher in R-CNRM (~5.5 mg Chl m^{-3}). Note that MODIS and SeaWiFS satellite observations differ by ~1 mg Chl m^{-3} due to different algorithms (O'Reilly et al., 1998; Letelier and Abbott, 1996) and measurement time periods (cf section 2.6). RCMs are able to correct the ESM inability to represent nearshore surface chlorophyll concentration (Fig. 12b). Moderate positive trends are found in R-IPSL (+13%, Table 4) and R-GFDL (+11%), which is quite surprising given the nitracline deepening (Fig. 11c). Strong multidecadal variability with almost no trend is found in R-CNRM. The ESM trends display very different patterns (Fig. 12b). ESM surface chlorophyll decreases in all cases, with strong negative trends (between -11% and -104%), a behavior not simulated in the RCMs.

The total chlorophyll content, depth-integrated over 0-500m (which includes the euphotic layer) (Fig. 12c), displays weak trends in R-IPSL (-1%, Table 4) and R-GFDL (+3%) and a moderate decrease in R-CNRM (-8%). The RCM weak trends agree relatively with the moderate decrease (-3%) found in two of the ESMs (IPSL and GFDL, Fig. 12d). However, the R-CNRM downtrend is weaker (-8%) with respect to CNRM (-32%).

The different evolution of the RCM surface and total chlorophyll content implies that the vertical distribution of phytoplankton biomass is modified in the long term. The vertical and cross-shore structure of chlorophyll trends indicates that all RCMs simulate a chlorophyll increase in the surface layer near the coast, and a decrease below ~5 m (Figs. 13a-c). Interestingly, this suggests that total biomass changes can not be monitored using satellite measurements, as the subsurface plankton depletion can not be observed. These results are consistent with a shoaling of the mixed layer (Fig. 7), which reduces



395 light limitation of phytoplankton growth (e.g. Echevin et al., 2008; Espinoza-Morriberon et al., 2017) and increases surface
primary productivity. The apparent correlation between decadal variability of the chlorophyll content and nitracline depth in
R-CNRM (e.g. the oscillations in 2070-2100 in Fig.12c) suggests that limitation of phytoplankton growth by nitrate uptake
may also play a role.

To further investigate the drivers of the surface chlorophyll trends, RCM and ESM primary productivity (PP) trends are
shown in Fig.14. RCM PP surface trends are weak (between -6% and +6%). In particular, the weak negative trend in R-IPSL
400 (-4%) is at odds with the surface chlorophyll increase (+13%, Fig.12a). In all RCMs, PP is strongly impacted by decadal
variability as a consequence of upwelling (Fig.5a) and nitracline depth variability (Fig.11c). These surface trends contrast
with the more pronounced ESM trends, in particular for IPSL (-25%) and CNRM (-113%). However, one may wonder the
meaning of the ESM trends when associated with very weak chlorophyll concentrations (Figs.12b,d). The RCM depth-
integrated PP trends are consistent with those of surface PP but differ from the ESMs, especially for R-CNRM (-7%) and
405 CNRM(-66%).

Overall, the contrasted trends found in the RCMs and ESMs, even when a similar biogeochemical model is used (e.g.
PISCES in IPSL and CNRM), illustrate the necessity to regionally downscale ESM variability to reduce systematic bias and
better represent local processes impacting on productivity.

410

Zooplankton biomass variations

The two zooplankton groups represented by RCMs are aggregated in a single group to allow a comparison with the
ESMs. RCM surface zooplankton display different evolutions than phytoplankton. First multidecadal variability is quite
strong and trends are weak. Zooplankton slightly accumulates in R-GFDL (+4%, Fig.15a, Table 4) and slightly reduces in R-
415 CNRM (-4%), in line with the trends of surface phytoplankton available for grazing (+11% in R-GFDL and -1% in R-GFDL,
Fig.12a). In contrast, surface zooplankton is relatively stable in R-IPSL in spite of a marked surface phytoplankton increase
(+13%). These weak zooplankton trends contrast with the strong ESM downtrends (from -15% in GFDL to -98% in CNRM,
Fig.15b). Depth-integrated zooplankton biomass decreases moderately in all RCMs, from -2% in R-GFDL to -8% in R-IPSL
(Fig.15c). Note that the decrease is non linear in R-IPSL and accelerates after 2050. As for surface zooplankton, the ESM
420 depth-integrated zooplankton downtrends are much stronger than the RCMs, e.g. reaching -56% in CNRM vs -6% in R-
CNRM. This suggests that zooplankton downtrends in ESMs may be overestimated due to unresolved local processes in the
coarse-grid models. As for chlorophyll, the trends vary significantly over the vertical (Figs.16d-f), suggesting that monitoring
of zooplankton at surface and subsurface must be carried out to follow climate-induced evolutions.

425

4 Summary and discussion

4.1 Summary of the main results

The dynamical downscaling of the ocean circulation and ecosystem functioning for three ESMs is performed in the
NHCS for the strongly warming, so-called “business-as-usual” RCP8.5 climate scenario. The RCM simulations all show an
intense warming of the surface layer within 100 km from the Peruvian coasts, reaching between +2°C and +4.5°C in 2100.



430 The nearshore surface warming is closely associated with a subsurface warming in the near-equatorial region (95°W, 2°N-10°S) which propagates into the NHCS. The coastal warming is weakest when the wind-driven upwelling is maintained (e.g. in R-GFDL), and strong when it is reduced (e.g. in R-IPSL and R-CNRM, see also Echevin et al., 2013; Oerder et al., 2015). The coastal warming found in the RCMs is close to that found in the ESMs, but surface and subsurface temperature mean biases (for the period 2006-2015) are greatly reduced in the RCMs.

435 Biogeochemical trends from the RCMs and ESMs are compared. The RCM simulations display a decrease of the near-equatorial (95°W, 2°N-10°S) eastward oxygen flux into the NHCS, associated with a slowdown of the eastward equatorial circulation. Strong deoxygenation occurs in the nearshore region only when the eastward oxygen flux is strongly reduced. Nutrient supply from the near-equatorial region to the NHCS decreases in all RCMs due to progressive nitrate depletion of equatorial waters and to decreasing eastward flux. This drives a deepening of the nearshore nitracline in two RCMs, but a
440 weak nitracline shoaling can occur if wind-driven coastal upwelling is maintained.

Chlorophyll concentration displays contrasted coastal trends. First, in all RCMs, surface chlorophyll does not decrease, in contrast with strong ESM downtrends (from -11% to -104%). Surface chlorophyll even increases markedly (>10%) in two RCMs, while the total chlorophyll biomass remains stable, indicating an enhanced stratification of phytoplankton in the surface layer in 2100. Total phytoplanktonic biomass (i.e. integrated over the water column) in the
445 coastal zone may also remain stable in spite of a slightly decreasing primary productivity driven by a weakening upwelling and deepening nutricline. This counterintuitive evolution can be partly driven by the reduced offshore transport (related to coastal upwelling) which allows floating organisms to accumulate in the coastal band. This would also induce a greater residence time of phytoplankton in the coastal area hence a stronger prey availability favoring grazing and a larger zooplankton biomass. However, the total zooplankton biomass tends to decrease in all RCMs, which shows that complex
450 nonlinear effects (e.g. temperature, prey and predation relations) drive plankton trends. Note that RCM zooplankton downtrends are weaker than the ESM downtrends used to drive fish global models (e.g. Tittensor et al., 2018). In the following subsections we discuss in more details the surface temperature trends, the near-equatorial conditions impacting the NHCS and the impact of the downscaling on the plankton trends.

455 4.2 SST warming

Enhanced surface heat fluxes and coastal upwelling of offshore-warmed source waters appear to be the main drivers of the nearshore SST evolution. The strongest nearshore warming (+4.5°C in 2100) found in R-IPSL likely results from the superposition of four effects: (i) a stronger warming of subsurface waters in the near-equatorial region subsequently transported towards the coastal region, (ii) a reduced cooling due to a decreasing coastal upwelling driven by the wind
460 relaxation, (iii) a stable shortwave flux and (iv) an increasing downward longwave flux due to the greenhouse effect. Moreover, IPSL-CM5 ranks among the high-sensitivity climate models of CMIP5 due to a large positive low-level clouds feedback (Brient and Bony, 2013). The weaker surface warming in R-CNRM (+3.5°C in 2100) may be mitigated by the weaker insolation. Last, the weakest warming in R-GFDL (+2°C in 2100) can be explained by (i) the weakest offshore subsurface temperature anomalies, (ii) the strongest wind-driven coastal upwelling (which brings deeper colder waters to the
465 surface layer) and (iii) the weakest greenhouse forcing. As upwelling-favorable winds are more likely to decrease than to



increase in low-latitude EBUS such as the Peruvian system (Goubanova et al., 2011; Belmadani et al., 2014; Rykacsewski et al., 2015), an upwelling reduction and strong SST warming appears to be the most robust projection. However, a rigorous estimate of the forcing terms in the nearshore heat budget would necessitate the online computation of each term (e.g. Echevin et al., 2018). Unfortunately, this could not be done in these 100-year long simulations because of the high
470 computational time cost and storage space.

Warmer surface waters may have severe consequences on the functioning of the Humboldt current ecosystem as a whole (Doney, 2006; Doney et al., 2012). In spite of the broad temperature range in which small pelagic fish species (e.g. anchovy, sardine or jack mackerel) are found (e.g. Gutierrez et al., 2008), the temperature anomalies associated with El Niño
475 events may drive the NHCS into conditions detrimental for pelagic recruitment. Moreover, previous modelling studies based on the RCP8.5 scenario suggest that peruvian fisheries will be impacted by the poleward migration of exploited species to encounter cooler waters (e.g. Cheung et al., 2018).

4.3 Near-equatorial eastward flow and OMZ variability

480 Eastward EUC and SSCCs appear to be strong drivers of OMZ variability as they transport relatively oxygenated equatorial waters into the OMZ (Cabr e et al., 2015; Shigemitsu et al., 2017; Montes et al., 2014; Espinoza-Morriberon, 2018; Busecke et al., 2019). The EUC is supposed to be mainly forced by the zonal pressure gradient across the equatorial Pacific, associated to the trade winds and the Walker circulation (hereafter WC; Stommel, 1960). However, most of the CMIP5 climate models fail to reproduce the WC intensification observed in the recent period (1980-2010) (e.g. Kociuba and Power,
485 2015). Furthermore, the EUC decrease in the eastern equatorial Pacific found in GFDL and in IPSL (respectively -26% and -22% decrease between 2005 and 2100 for the mean velocity between 2°N and 2°S, 95°W, 50-200 m depth, Figure not shown) is not consistent with RCP8.5 WC trends reported in Kociuba and Power (2015). EUC trends also vary a great deal across the equatorial Pacific (Drenkard and Karnauskas, 2014). EUC dynamics is likely sensitive to stratification changes in the equatorial thermocline (McCreary, 1981). To our knowledge, the drivers of EUC long-term variability in the eastern
490 equatorial Pacific are not well known.

Besides, the drivers of SSCC variability, which also contribute to the NHCS trends, are not well known. The primary SSCC (near 4°-6°S at 90°W) is supposed to be forced partly by trade winds and alongshore winds in the NHCS, by exchanges between the Pacific basin and the Indian ocean, and by surface heating in the tropics (Furue et al., 2007). Furthermore, SSCCs are not resolved in CMIP5 models, likely due to the ocean model coarse resolution (e.g. see Fig.4 in
495 Cabr e et al., 2015). This implies that the oxygenation trend in the NHCS OMZ is difficult to project using the current generation of ESMs.

Besides, ventilation of the OMZ by the near-equatorial eastward currents does not appear to be the dominating process driving oxygen variability in our simulations. Indeed, the oxycline trends have different signs in R-CNRM and R-IPSL (Figs.10a,b) in spite of the weakly decreasing eastward flow of oxygen, possibly owing to different biogeochemical
500 processes. The nearshore nitracline deepens dramatically due to nutrient depletion of equatorial water masses in R-CNRM (Fig.11). This nitrate decline drives a downtrend of primary production (Fig.13a,c) and export of organic matter (hereafter



OM) out of the euphotic layer (not shown). This results in a reduction of OM respiration, which may contribute to the oxygenation of the subsurface layers and oxycline deepening (Fig.10a,b). Conversely, deoxygenation could be enhanced as biomass accumulates in the coastal areas (e.g. in R-GFDL, Fig.12c), increasing downward export of OM and subsurface respiration. However, a rigorous budget of oxygen in the coastal region is needed to confirm the respective impact of these mechanisms.

As mentioned in section 2.5, all RCMs are forced by climatological seasonally-varying WOA DO concentrations at the model boundaries, because of a seemingly unrealistically high oxygenation trend in CNRM-CM5 (Fig.17a) with respect to observed trends in the last 50 years (Stramma et al., 2008). To investigate the impact of the actual ESM oxygen trends, sensitivity experiments (named R-GCM') were performed. The protocol was similar to the one described in section 2, except for the OBC that were forced using the ESM oxygen trends. Because of the very weak downtrend of the near-equatorial eastward flow (Fig.9a) and of a strong oxygenation (+38%) (Fig.17a), an unrealistic, very strong oxygenation trend is found in the nearshore region for R-CNRM' (Fig.17c). However, it is notable that the marked deoxygenation of subsurface coastal waters in R-GFDL (-39%, Fig.10b) is almost stalled in R-GFDL' (-4%). This suggests that a weak oxygenation of near-equatorial water masses (+5%, Fig.17a) may compensate the impact of the circulation slowdown (Fig.7a) and enable a rather stable oxygen flux to the NHCS (Fig.17b). In other words, NHCS nearshore oxygen trends depend not only on local processes (locally produced organic matter, coastal upwelling,...) but also on subtle variability of remote processes in ESMs such as deoxygenation (Stramma et al.,2008; Oschlies et al., 2018) and EUC trends (Shigemitsu et al., 2017) in the eastern Equatorial Pacific. A better representation of the OMZ in ESMs is thus a key preliminary requirement for future regional studies in the NHCS.

4.4 Plankton trends

A stable and, in one case, increasing concentration of chlorophyll are found in the surface layer (0-5m), in spite of primary production decrease (e.g. in R-CNRM and R-IPSL, Fig.14). Several mechanisms could contribute to partly compensate the PP decrease.

The shoaling of the mixed layer may constrain phytoplankton vertically and increase surface concentration. The increased temperature in the near-surface layer (0-50 m depth) induces a faster growth rate of phytoplankton cells (Eppley, 1972). Furthermore, the decrease of upwelling and offshore export (Fig.5) may concentrate more biomass in the coastal region and contribute to the phytoplankton persistence in R-IPSL and R-CNRM. However, performing a budget of phytoplankton in the model is needed to estimate precisely the relative contribution of each process, which is beyond the scope of the present study.

Examination of RCM zooplankton biomass shows weak trends (between -4% and 4%) in the surface layer and weak downtrends (between -2% and -8%) for total biomass (Fig.15). R-IPSL and R-GFDL zooplankton biomass decrease faster than phytoplankton, which corresponds to a trophic attenuation of the transfer of biomass to upper levels. A similar attenuation has been found in regional simulations of the Benguela upwelling system under the IPCC-AR4 A1B scenario (corresponding to the more moderate RCP6.0 scenario) (Chust et al., 2014). The RCM zooplankton trends also contrast with the very strong ESM downtrends. These discrepancies can be attributed to local physical processes (transport and mixing



associated to the mesoscale) not represented in the ESMs, but also partly to the use of an earlier version of the ecosystem model (PISCES) run with a set of biogeochemical parameters adapted for the NHCS (see Table 1 in Echevin et al., 2013).
540 The stronger total zooplankton biomass downtrends in R-CNRM and R-IPSL suggest a strong impact of the temperature increase, possibly due to the higher zooplankton mortality in a warmer environment. However, the model's microzooplankton and mesozooplankton result from a nonlinear interplay of temperature and predation/mortality effects. Further interpretation of these trends would require dedicated sensitivity experiments and performing a zooplankton budget. This is beyond the scope of the present study which aims to present an overview of the main low trophic level trends.

545

5 Conclusions

Regional downscaling of three ESMs is performed in the NHCS over the 21st century so-called "business-as-usual" RCP8.5 climate scenario using a regional coupled biodynamical model. All regional simulations reproduce an intense warming (2-4.5°C) of the surface layer in the upwelling region off central Peru, within 100 km from the coasts. The surface
550 warming is strongest for the two RCMs in which the wind-driven coastal upwelling weakens in the future. The downscaling procedure allows to correct model bias and the RCM physical trends are consistent with those obtained from the coarse-grid ESMs.

The biogeochemical impacts of climate change are more contrasted among RCMs. A slowdown of the eastward near-equatorial circulation reduces the ventilation of the NHCS, inducing a nearshore deoxygenation trend. However the long-term
555 variability of oxygen content of equatorial water masses can also impact the nearshore oxygen trends. As observed deoxygenation trends in the eastern equatorial Pacific are not well reproduced by ESMs (Stramma et al., 2008, 2012) and CMIP5 ESM systematic biases are strong in this region (Cabr e et al., 2015; Oschlies et al., 2018), these shortcomings limit the predictability of downscaled oxygen trends in the NHCS. One important conclusion of this study is that reducing the biases in oxygen concentration and zonal circulation trends in the eastern Equatorial Pacific ocean is crucial to project the
560 future evolution of the NHCS oxygen minimum zone.

Downscaled surface chlorophyll in the coastal region does not decrease, in contrast with the ESMs. In two RCMs, the surface chlorophyll remains high in the coastal region for two reasons: the enhanced thermal stratification due to the warming alleviates light limitation and vertical dilution, and the reduction of wind-driven offshore transport allows plankton to accumulate near the coast. These processes partly compensate the reduction of primary productivity due to a deeper nitracline
565 and reduced upwelling. Downscaled zooplankton trends are weak, and downtrends strengthen when the warming is stronger. In all RCMs, downscaled plankton trends differ markedly from those simulated by ESMs, illustrating the strong impact of the regional dynamical downscaling. This also highlights the necessity to interpret ESM biomass-based regional projections of fisheries (e.g. FISHMIP, Tittensor et al., 2018) with great caution.

As previous works point to a relaxation of upwelling-favorable wind conditions in the NHCS, dynamically
570 downscaled wind projections as well as more realistic large scale dynamical and biogeochemical conditions in the near-equatorial regions are needed to improve the robustness of our results in future studies. Furthermore, many aspects of the regional impact of climate change have not been explored, such as for example interannual variability associated with ENSO in a warmer NHCS or the acidification of coastal waters. These impacts will be addressed in future studies.



575 **Acknowledgements:**

Earth System Model output were downloaded from the ESGF website (<https://esgf-data.dkrz.de/search/cmip5-dkrz/>) and from the ciclad server at the Institut Pierre-Simon Laplace (IPSL). Regional simulations were performed on the ADA supercomputer at IDRIS (project n° A0050101140) and on the IMARPE Cluster. V. Echevin, F. Colas and M. Gévaudan were funded by IRD (Institut de Recherche pour le Développement), in particular by the IRD DISCOH program. The Inter-
580 American Development Bank (IDB) is acknowledged for funding the IMARPE cluster through project “Adaptación al Cambio Climático del Sector Pesquero y del Ecosistema Marino Costero del Perú”. J. Ramos is acknowledged for for administrating the IMARPE cluster. R. Soto is acknowledged for downloading the Earth System Model output.

References:

- 585 Aumont, O., Ethé, C., Tagliabue, A., Bopp, L., and Gehlen, M.: PISCES-v2: an ocean biogeochemical model for carbon and ecosystem studies. *Geosci. Model. Dev.* 8, 2465–2513. doi: 10.5194/gmd-8-2465-2015, 2015.
- Bakun, A. : Global climate change and intensification of coastal ocean upwelling. *Science* 247:198–201, 1990.
- Bakun, A., Field, D.B., Redondo-Rodriguez, A. and Weeks, S.J. : Greenhouse gas, upwelling-favorable winds, and the future of coastal ocean upwelling ecosystems. *Global Change Biology* (2010)16, 1213–1228, doi: 10.1111/j.1365-
590 2486.2009.02094.x, 2010.
- Belmadani, A., Echevin, V., Codron, F., Takahashi, K., and Junquas, C.: What dynamics drive future winds scenarios off Peru and Chile?, *Clim. Dyn.*, 43(7–8), 1893–1914, doi:10.1007/s00382-013-2015-2, 2014.
- Bertrand, A., Chaigneau, A., Peraltilla, S., Ledesma, J., Graco, M., Monetti, F., and Chavez, F. P.: Oxygen: a fundamental property regulating pelagic ecosystem structure in the coastal southeastern tropical Pacific. *PloS one*, 6(12), e29558,
595 2011.
- Brient, F., and Bony, S.: Interpretation of the positive low-cloud feedback predicted by a climate model under global warming. *Clim. Dyn.*, 40, 2415–2431, 2013.
- Brochier, T., Echevin, V., Tam, J., Chaigneau, A., Goubanova, K., and Bertrand, A.: Climate change scenario experiment predict a future reduction in small pelagic fish recruitment in the Humboldt Current system, *Global Change Biol.*, 19,
600 1841–1853, doi:10.1111/gcb.12184, 2013.
- Busecke, J. J. M., Resplandy, L., and Dunne, J. P. P.: The Equatorial Undercurrent and the oxygen minimum zone in the Pacific. *Geophysical Research Letters*, 46, 6716–20, 2124–2139, doi: 10.1111/gcb.125626725. <https://doi.org/10.1029/2019GL082692>, 2019.
- Cabré, A., Marinov, I., Bernardello, R., and Bianchi, D.: Oxygen minimum zones in the tropical Pacific across CMIP5
605 models: mean state differences and climate change trends. *Biogeosciences*, 12(18), 5429–5454, 2015.
- Cambon, G., Goubanova, K., Marchesiello, P., Dewitte, B., and Illig, S.: Assessing the impact of downscaled winds on a regional ocean model simulation of the Humboldt system, *Ocean Modell.*, 65, 11–24, doi:10.1016/j.ocemod.2013.01.007, 2013.
- Carton, J.A., and Giese, B.S.: A reanalysis of ocean climate using Simple Ocean Data Assimilation (SODA). *Mon. Weather*



- 610 Rev. 136, 2999–3017. <http://dx.doi.org/10.1175/2007MWR1978.1>, 2008.
- Chavez, F., Bertrand, A., Guevara-Carrasco, R., Soler, P., and Csirke J.: The northern Humboldt Current System: Brief history, present status and a view towards the future, *Prog. Oceanogr.*, 79, 95–105, doi:10.1016/j.pocean.2008.10.012, 2008.
- Cheung, W.W.L., Bruggeman, J., and Butenschön, J.: Projected changes in global and national potential marine fisheries catch under climate change scenarios in the twenty-first century. In *Impacts of climate change on fisheries and aquaculture: Synthesis of current knowledge, adaptation and mitigation options*. Food and Agriculture Organization of United Nation, 2018.
- 615
- Chust, G., et al.: Biomass changes and trophic amplification of plankton in a warmer ocean. *Global Change Biology*, 20(7), 2124–2139, doi: 10.1111/gcb.12562, 2014.
- 620 Czeschel, R., Stramma, L., Schwarzkopf, F. U., Giese, B. S., Funk, A., and Karstensen, J.: Middepth circulation of the eastern tropical South Pacific and its link to the oxygen minimum zone. *J. Geophys. Res.* doi: 10.1029/2010JC006565, 2011.
- Da Silva, A. M., Young, C. C., and Levitus, S.: *Atlas of Surface Marine Data 1994, vol. 1, Algorithms and Procedures*, Technical Report. Washington, D.C: U.S. Department of Commerce, 1994.
- de Boyer Montégut, C., Madec, G., Fischer, A. S., Lazar, A. and Iudicone, D.: Mixed layer depth over the global ocean: An examination of profile data and a profile-based climatology, *J. Geophys. Res.*, 109, C12003, doi:10.1029/2004JC002378, 2004.
- 625
- Doney, S.C.: Plankton in a warmer world. *Nature*, 444, 695–696. <https://doi.org/10.1038/444695a>, 2006.
- Doney, S.C., Ruckelshaus, M., Emmett Duffy, J. et al.: Climate Change Impacts on Marine Ecosystems. *Annual Review of Marine Science*, 4, 11–37. doi: 10.1146/annurev-marine-041911-111611, 2012.
- 630 Drenkard, E. J., and Karnauskas, K. B.: Strengthening of the Pacific equatorial undercurrent in the SODA reanalysis: Mechanisms, ocean dynamics, and implications. *Journal of Climate*, 27(6), 2405–2416, 2014.
- Echevin, V., Aumont, O., Ledesma, J., and Flores, G.: The seasonal cycle of surface chlorophyll in the Peruvian upwelling system: a model study. *Prog. Oceanogr.* 79, 167–176. doi: 10.1016/j.pocean.2008.10.026, 2008.
- Echevin, V., Colas, F., Chaigneau, A., and Penven, P.: Sensitivity of the Northern Humboldt Current System nearshore modeled circulation to initial and boundary conditions, *J. Geophys. Res.*, 116, C07002, doi:10.1029/2010JC006684, 2011.
- 635
- Echevin, V., Albert, A., Lévy, M., Aumont, O., Graco, M., and Garric, G.: Remotely-forced intraseasonal variability of the Northern Humboldt Current System surface chlorophyll using a coupled physical-ecosystem model. *Cont. Shelf. Res.* 73, 14–30. doi: 10.1016/j.csr.2013.11.015, 2014.
- Echevin, V., Colas, F., Espinoza-Morriberon, D., Vasquez, L., Anculle, T. and Gutierrez, D.: Forcings and Evolution of the 2017 Coastal El Niño Off Northern Peru and Ecuador. *Front. Mar. Sci.* 5:367. doi: 10.3389/fmars.2018.00367, 2018.
- 640
- Eppley, R. W.: Temperature and phytoplankton growth in the sea. *Fish. Bull.* 70(4), 1063–1085, 1972.
- Espinoza-Morriberón, D., Echevin, V., Colas, F., Tam, J., Ledesma, J., Vásquez, L., et al.: Impacts of El Niño events on the Peruvian upwelling system productivity, *J. Geophys. Res. Oceans*. 122, 5423–5444, doi: 10.1002/2016JC012439, 2017.
- Espinoza-Morriberón, D., Echevin, V., Colas, F., Tam, J., Gutierrez, D., Graco, M., Ledesma, J. and Quispe-Ccalluari, C.: Oxygen Variability During ENSO in the Tropical South Eastern Pacific, *Front. Mar. Sci.* 5:526, doi: 10.3389/fmars.2018.00526, 2018.
- 645



- 2019.
- Espinoza-Morriberón, D. (2018). Variabilité interannuelle et décennale de la productivité et de la zone de minimum d'oxygène dans le système d'upwelling du Pérou, PhD dissertation, Sorbonne University, Paris, France.
- Ferry, N., et al.: GLORYS2V1 global ocean reanalysis of the altimetric era (1992–2009) at meso scale, Mercator Ocean–
650 Quaterly Newsletter, 44, 2012.
- Furue, R., McCreary, J. P., Yu, Z., and Wang, D.: The dynamics of the southern Tsuchiya Jet, *J. Phys. Oceanogr.*, 37, 531–553, doi:10.1175/JPO3024.1, 2007.
- Flato, G., et al.: Evaluation of climate models. *Climate Change 2013: The Physical Science Basis. Contribution of Working Group I to the Fifth Assessment Report of the Intergovernmental Panel on Climate Change*, edited by T. F. Stocker et al.,
655 pp. 741–866, Cambridge Univ. Press, Cambridge, U. K., and New York., doi:10.1017/CBO9781107415324.020, 2013.
- Franco, A. C., Gruber, N., Frolicher, T. L., and Kropuenske Artman, L.: Contrasting impact of future CO₂ emission scenarios on the extent of CaCO₃ mineral undersaturation in the Humboldt Current System, *Journal of Geophysical Research: Oceans*, 123. <https://doi.org/10.1002/2018JC013857>, 2018.
- Goubanova, K., Echevin, V., Dewitte, B., Codron, F., Takahashi, K., Terray, P. and Vrac, M.: Statistical downscaling of sea-
660 surface wind over the Peru–Chile upwelling region: diagnosing the impact of climate change from the IPSL–CM4 model, *Clim Dyn*, doi:10.1007/s00382-010-0824-0,2010.
- Grados, C., Chaigneau, A., Echevin, V. and Domínguez, N.: Upper ocean hydrology of the Northern Humboldt Current System at seasonal, interannual and interdecadal scales, *Progress in Oceanography* 165, 123–144, 2018.
- Graco M., Anculle, T., Chaigneau A., Ledesma J., Flores G., Morón, O., Monetti F., and D. Gutiérrez: Variabilidad espacial y
665 temporal del oxígeno disuelto y de la ZMO en el sistema de afloramiento frente a Perú. *Boletín Instituto del Mar del Perú, Volumen Especial*, 2018.
- Gutiérrez, D., Bouloubassi, I., Sifeddine, A., Purca, S., Goubanova, K., Graco, M., Field, D., Méjanelle, L., Velazco, F., Lorre, A., Salvatelli, R., Quispe, D., Vargas, G., Dewitte, B., and Ortlieb, L.: Coastal cooling and increased productivity in the main upwelling zone off Peru since the mid-twentieth century, *Geophys. Res. Lett.*, 38, L07603,
670 doi:10.1029/2010GL046324, 2011.
- Gutierrez, M., Ramirez, A., Bertrand, S., Moron, O. and Bertrand, A.: Ecological niches and areas of overlap of the squat lobster ‘munida’ (*Pleuroncodes monodon*) and anchoveta (*Engraulis ringens*) off Peru, *Progress in Oceanography*, 79, 256–263.,2008.
- Kociuba, G., and Power, S. B.: Inability of CMIP5 models to simulate recent strengthening of the Walker circulation: Implications for projections, *Journal of Climate*, 28(1), 20–35,2015.
- Letelier, R. M., and Abbott, M. R.: An analysis of chlorophyll fluorescence algorithms for the Moderate Resolution Imaging Spectrometer (MODIS), *Remote Sensing of Environment*, 58(2), 215–223, 1996.
- L’Heureux, M., Lee, S. and Lyon, B.: Recent multidecadal strengthening of the Walker circulation across the tropical Pacific. *Nature Climate Change*, 3, 571–576, 2013.
- 680 Liu, W. T., Katsaros, K. B., and Businger, J. A.: Bulk parameterization of air– sea exchanges of heat and water vapor including the molecular constraints at the interface, *J. Atmos. Sci.* 36, 1722–1735, doi: 10.1175/1520-



- 0469(1979)036<1722:BPOASE>2.0.CO;2, 1979.
- Luyten, J.R., Pedlosky, J., and Stommel, H.: The Ventilated Thermocline, *J. Phys. Oceanogr.*, 13, 292–309, [https://doi.org/10.1175/1520-0485\(1983\)013<0292:TVT>2.0.CO;2](https://doi.org/10.1175/1520-0485(1983)013<0292:TVT>2.0.CO;2), 1983.
- 685 McCreary, J.P.: A linear stratified ocean model of the equatorial undercurrent, *Philosophical Transactions of the Royal Society of London*. Vol.298, 1444, <https://doi.org/10.1098/rsta.1981.0002>, 1981.
- Mogollón, R., and Calil, P.H.: Counterintuitive effects of global warming-induced wind patterns on primary production in the northern Humboldt current system, *Glob.Chang. Biol.*, 24 (7), 3187–3198. <https://doi.org/10.1111/gcb.14171>, 2018.
- 690 Montes, I., Colas, F., Capet, X., and Schneider, W.: On the pathways of the equatorial subsurface currents in the eastern equatorial Pacific and their contributions to the Peru–Chile Undercurrent, *J. Geophys. Res. Oceans*, 115:C09003. doi: 10.1029/2009JC005710, 2010.
- Montes, I., Dewitte, B., Gutknecht, E., Paulmier, A., Dadou, I., Oschlies, A., et al.: High-resolution modeling of the Eastern Tropical Pacific Oxygen Minimum Zone: sensitivity to the tropical oceanic circulation, *J. Geophys. Res. Oceans*, 119, 5515–5532. doi: 10.1002/2014JC009858, 2014.
- 695 Oerder, V., Colas, F., Echevin, V., Codron, F., Tam, J. and Belmadani, A.: Peru–Chile upwelling dynamics under climate change, *J. Geophys. Res. Oceans*, 120, 1152–1172, doi:10.1002/2014JC010299, 2015.
- O'Reilly, J. E., Maritorena, S., Mitchell, B. G., Siegel, D. A., Carder, K. L., Garver, S. A. et al.: Ocean color chlorophyll algorithms for SeaWiFS, *Journal of Geophysical Research: Oceans*, 103(C11), 24937–24953, 1998.
- Oschlies, A., Brandt, P., Stramma, L., & Schmidtko, S.: Drivers and mechanisms of ocean deoxygenation, *Nature geoscience*, 700 11(7), 467, 2018.
- Oyarzún, D., & Brierley, C. M.: The future of coastal upwelling in the Humboldt current from model projections. *Climate Dynamics*, 52(1-2), 599–615, 2019
- Penven, P., Debreu, L., Marchesiello, P., and McWilliams, J. C.: Evaluation and application of the ROMS 1-way embedding procedure to the central California upwelling system. *Ocean Modell.* 12, 157–187. doi: 10.1016/j.ocemod.2005.05.002, 705 2006.
- Penven, P., Echevin, V., Pasapera, J., Colas, F., and Tam, J.: Average circulation, seasonal cycle, and mesoscale dynamics of the Peru Current System: a modeling approach. *J. Geophys. Res. Oceans* 110. doi: 10.1029/2005JC002945, 2005.
- Penven, P., Marchesiello, P., Debreu, L., and Lefèvre, J.: Software tools for pre-and post-processing of oceanic regional simulations, *Environ. Model. Softw.*, 23, 660–662. doi: 10.1016/j.envsoft.2007.07.004, 2008.
- 710 Plesca, E., Grützun, V., and Buehler, S. A.: How robust is the weakening of the Pacific Walker circulation in CMIP5 idealized transient climate simulations?. *Journal of Climate*, 31(1), 81–97, 2018.
- Resplandy, L., Levy, M., Bopp, L., Echevin, V., Pous, S., Sarma, V. V. S. S., et al.: Controlling factors of the oxygen balance in the Arabian Sea's OMZ. *Biogeosciences* 9, 5095–5109. doi: 10.5194/bg-9-5095-2012, 2012.
- Ridgway, K. R., Dunn, J. R., and Wilkin, J. L.: Ocean interpolation by four-dimensional least squares—Application to the waters around Australia, *J. Atmos. Oceanic Technol.*, 19(9), 1357–1375, 2002.
- 715 Risien, C., and Chelton, D.: A global climatology of surface wind and wind stress fields from eight years of Quikscat scatterometer data, *J. Phys. Oceanogr.*, 38, 2379–2413, doi:10.1175/2008JPO3881.1, 2008.



- Rykaczewski, R. R., Dunne, J. P., Sydeman, W. J., García-Reyes, M., Black, B. A., and Bograd, S. J.: Poleward displacement of coastal upwelling-favorable winds in the ocean's eastern boundary currents through the 21st century, *Geophys. Res. Lett.*, 42, 6424–6431, doi:10.1002/2015GL064694, 2015.
- 720 Sanchez, S.: Variacion estacional e interanual de la biomasa fitoplanctonica y concentraciones de clorofila frente a la costa peruana durante 1976–2000, *Bol. Inst. Mar Peru*, 19(1–2), 29–43, 2000.
- Shchepetkin, A. F., and McWilliams, J. C.: Quasi-monotone advection schemes based on explicit locally adaptive dissipation. *Mon. Weather Rev.* 126, 1541–1580. doi: 10.1175/1520-0493(1998)126<1541:QMASBO>2.0.CO;2, 1998.
- 725 Shchepetkin, A. F., and McWilliams, J. C.: The regional oceanic modeling system (ROMS): a split-explicit, free-surface, topography-following-coordinate oceanic model. *Ocean Model.* 9, 347–404. doi: 10.1016/j.ocemod.2004.2005.
- Shchepetkin, A. F., and McWilliams, J. C.: Correction and commentary for “Ocean forecasting in terrain-following coordinates: formulation and skill assessment of the regional ocean modeling system” by Haidvogel et al., *Comp. J. Phys.*, 227, 3595–3624, 2009.
- 730 Shigemitsu, M., Yamamoto, A., Oka, A., and Yamanaka, Y.: One possible uncertainty in CMIP5 projections of low-oxygen water volume in the Eastern Tropical Pacific, *Global Biogeochem. Cycles*, 31, 804–820, doi:10.1002/2016GB005447, 2017.
- Smith, W. H., and Sandwell, D. T.: Global sea floor topography from satellite altimetry and ship depth soundings, *Science*, 277, 1956–1962, doi: 10.1126/science.277.5334.1956, 1997.
- 735 Stommel, H.: Wind-drift near the equator, *Deep Sea Res.* 6, 298–302, 1960.
- Stramma, L., Johnson, G. C., Sprintall, J., and Mohrholz, V.: Expanding Oxygen-Minimum Zones in the tropical oceans, *Science*, 320, 655–658, doi: 10.1126/science.1153847, 2008.
- Stramma, L., Schmidtko, S., Levin, L. A., and Johnson, G. C.: Ocean oxygen minima expansions and their biological impacts, *Deep Sea Research Part I: Oceanographic Research Papers*, 57(4), 587–595., 2010.
- 740 Thomsen, S., Kanzow, T., Colas, F., Echevin, V., Krahnemann, G., and Engel, A.: Do submesoscale frontal processes ventilate the oxygen minimum zone off Peru?, *Geophys. Res. Lett.*, 43, 8133–8142, doi:10.1002/2016GL070548, 2016.
- Tittensor, et al.: A protocol for the intercomparison of marine fishery and ecosystem models: Fish-MIP v1.0, *Geosci. Model Dev.*, 11, 1421–1442, <https://doi.org/10.5194/gmd-11-1421-2018>, 2018.
- 745 Tokinaga, H., and Xie, S. P.: Wave-and anemometer-based sea surface wind (WASWind) for climate change analysis, *Journal of Climate*, 24(1), 267–285, 2011.
- van Vuuren, D.P., Edmonds, J., Kainuma, M. et al.: The representative concentration pathways: an overview, *Climatic Change*, 109: 5. <https://doi.org/10.1007/s10584-011-0148-z>, 2011.
- Vecchi, G. A., and B. J. Soden: Global warming and the weakening of the tropical circulation, *J. Clim.*, 20, 4316–4340, doi:10.1175/JCLI4258.1, 2007.
- 750 Wang, D., Gouhier, T. C., Menge, B. A., & Ganguly, A. R.: Intensification and spatial homogenization of coastal upwelling under climate change. *Nature*, 518(7539), 390, 2015.

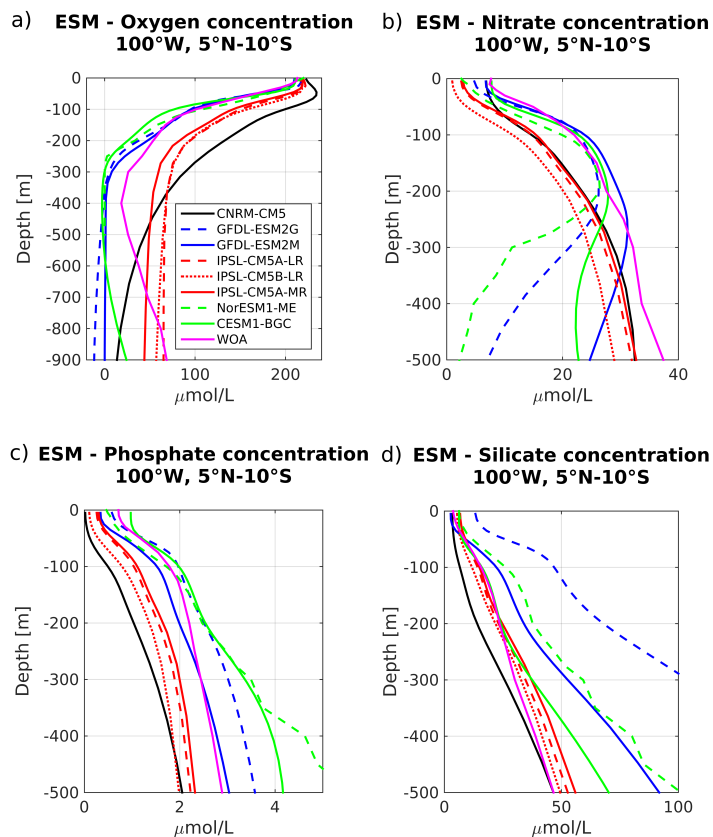


Figure 1: Vertical profiles of a) oxygen, b) nitrate, c) phosphate, d) silicate concentrations in the Eastern Equatorial Pacific Ocean for 8 Earth System Models (ESMs: CNRM-CM5 (black line), GFDL-ESM2M (blue line), GFDL-ESM2G (blue dashed line), IPSL-CM5A-MR (red line), IPSL-CM5A-LR (red dashed line), IPSL-CM5B-LR (red dotted line), CESM1-BGC (green line), Nor-ESM1-ME (green dashed line)). Tracer concentrations are averaged along 100°W between 5°N and 10°S . The three selected models are shown in thick colored lines. WOA observations are marked by magenta lines.

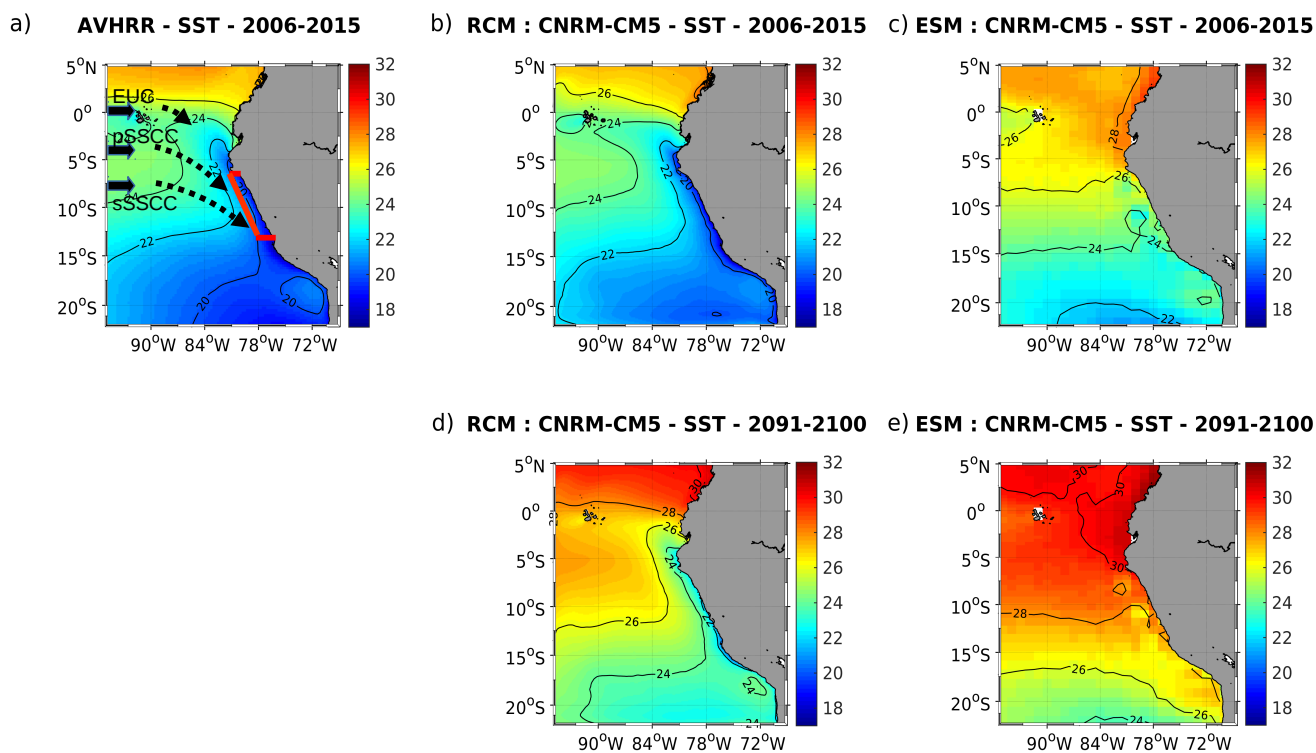


Figure 2: Annual mean SST (in °C) for (a) AVHRR surface observations (2006-2015), (b) CNRM-CM5 (Control period, 2006-2015), (c) CNRM-CM5 downscaled (2006-2015), (d) CNRM-CM5 (RCP8.5, 2091-2100), (e) CNRM-CM5 downscaled (RCP8.5, 2091-2100). The red box in (a) marks the coastal box in which surface and subsurface variables are averaged (see methodology section 2.8). Subsurface eastward equatorial currents (Equatorial Under Current (EUC) primary and secondary subsurface counter currents (pSSCC and sSSCC)) are sketched in (a).

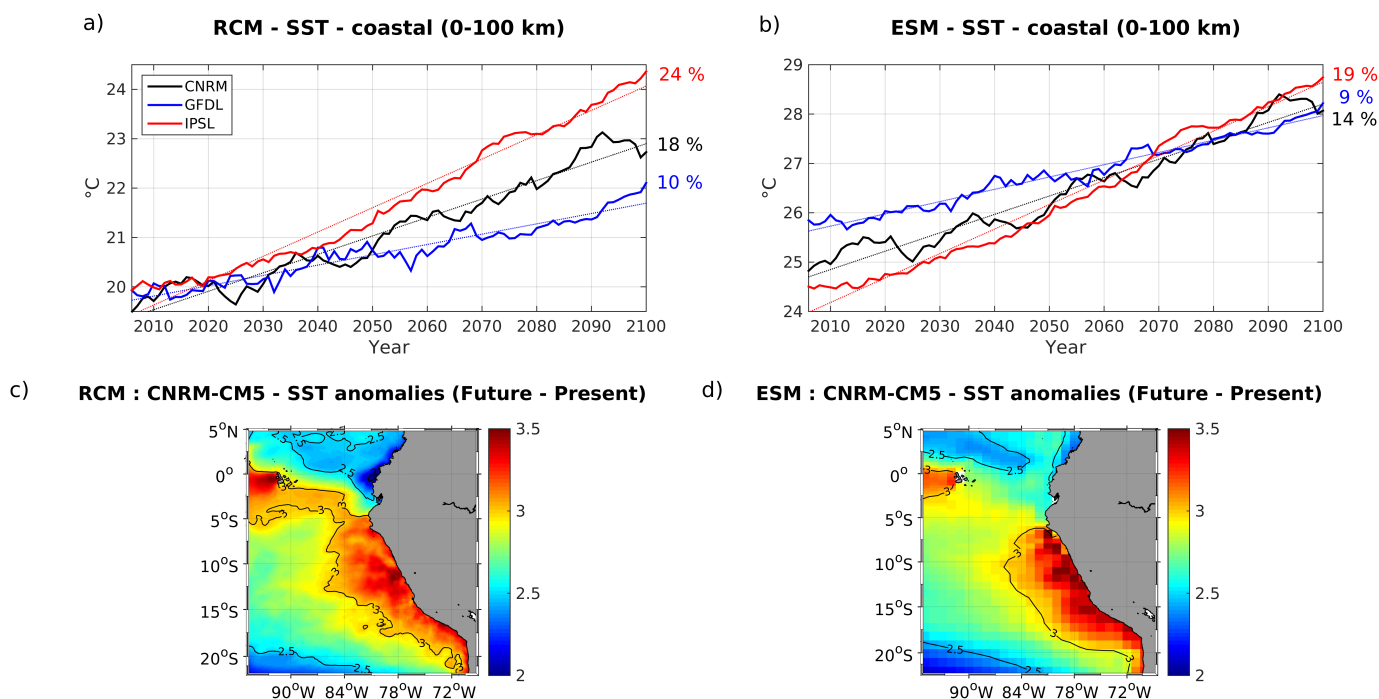


Figure 3: Coastal SST (in °C) in (a) the RCMs and (b) the ESMs (CNRM in black, GFDL in blue, IPSL in red). All fields are averaged in a coastal box (see Figure 2a) and annual mean time series are filtered using a 10-year moving average. Dotted lines indicate linear trends and percentage values indicate the change between 2006 and 2100 with respect to present conditions using the linear trend values (i.e. $100 \cdot (X(t=2100) - X(t=2006)) / X(t=2006)$ where $X(t)$ is the linear trend). (c) R-CNRM SST anomaly (2091-2100 average minus 2006-2015) and (d) CNRM SST anomaly (2091-2100 average minus 2006-2015).

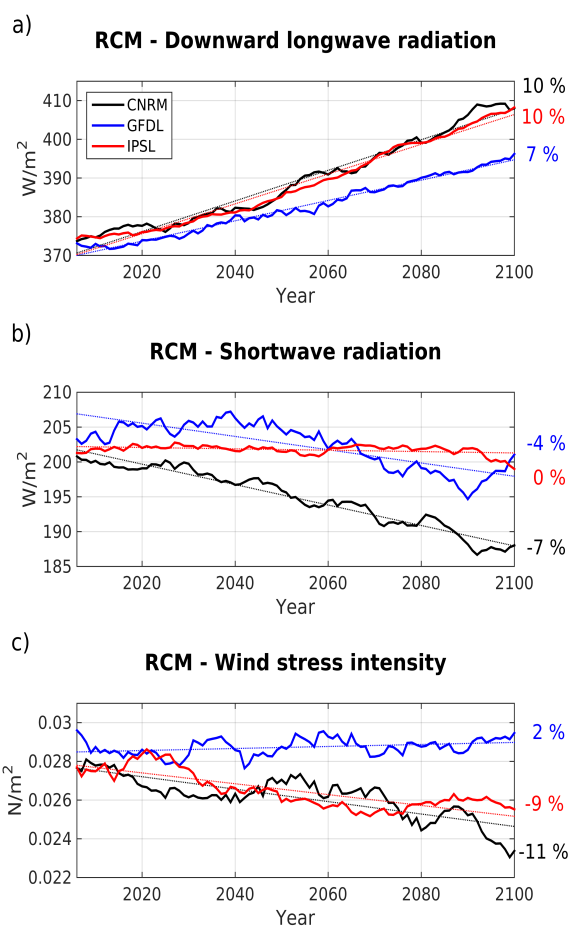


Figure 4: (a) Downward longwave radiation (in W m^{-2} , positive downward), (b) net downward shortwave radiation (in W m^{-2}), (d) alongshore wind stress (in N m^{-2}), for the three RCMs (CNRM in black, GFDL in blue, IPSL in red). All fields are averaged in a coastal box (see Figure 2a) and annual mean time series are filtered using a 10-year moving average.

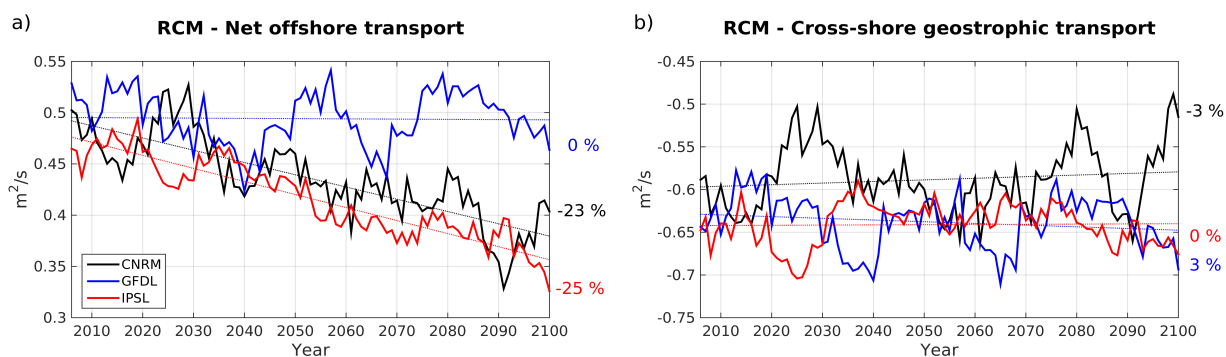


Figure 5: (a) Net offshore transport (in $\text{m}^2 \text{s}^{-1}$, positive offshoreward), vertically averaged in the Ekman layer, (b) cross-shore geostrophic transport compensating the wind-driven upwelling (in $\text{m}^2 \text{s}^{-1}$). The transports are averaged in a coastal box (see Figure 2a) for the three RCMs (CNRM in black, GFDL in blue, IPSL in red). Annual mean time series are filtered using a 10-year moving average.

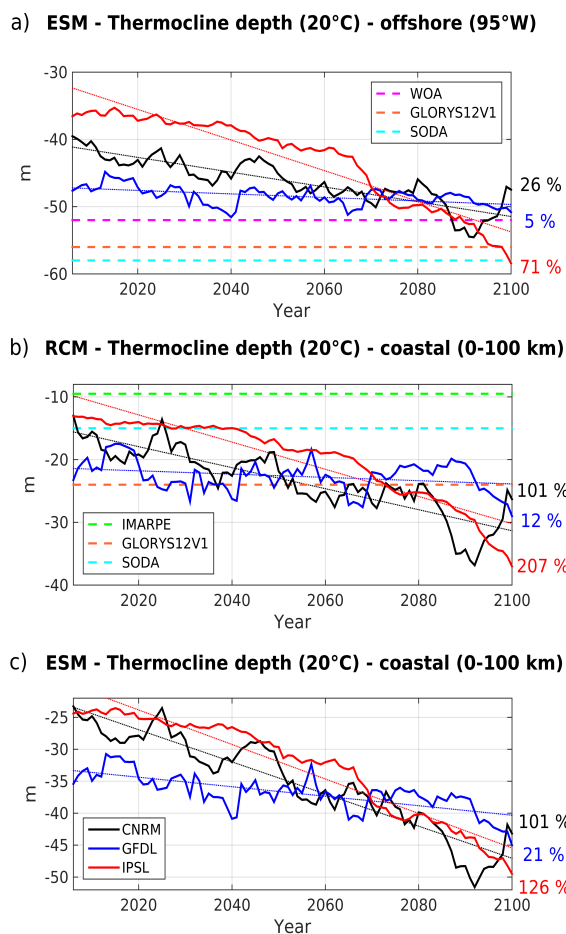


Figure 6: Depth of 20°C isotherm (D20, in meters) (a) at 95°W, averaged between 2°N-10°S, (b) in the coastal box for the three RCMs and (c) for the 3 ESMs (CNRM in black, GFDL in blue, IPSL in red). The timeseries are filtered using a 10-year moving average. Climatological D20 from WOA (dashed magenta line) and two reanalyses (dashed red line for GLORYS12V1 (1993-2017), dashed light blue line for SODA(1992-2000)) are also shown in (a). D20 from IMARPE climatology is marked by a dashed green line in (b). Annual mean time series are filtered using a 10-year moving average.

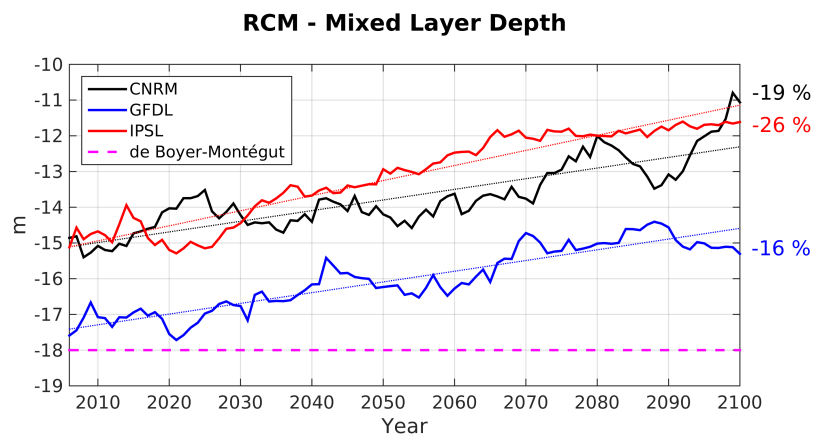


Figure 7: RCM mixed layer depth (in meters) in the RCMs (CNRM in black, GFDL in blue, IPSL in red). Annual mean time series are filtered using a 10-year moving average. The climatological value derived from the De BoyerMontegut et al. (2004) climatology is marked by a dashed magenta line.

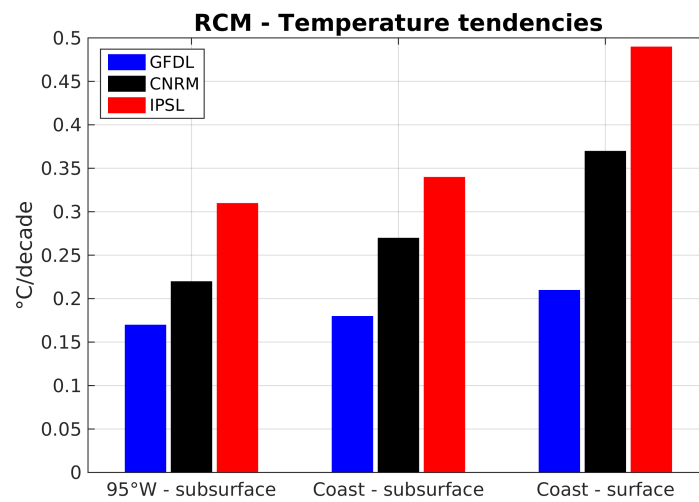


Figure 8: Depth-averaged RCM temperature linear trends between 2006 and 2100 (in °C/decade) in the equatorial region (95°W, 2°N-10°S, 50-200 m, left), in the coastal region (center) and in surface layer (0-5 m, right). CNRM, GFDL and IPSL trends are shown in black, blue and red, respectively.

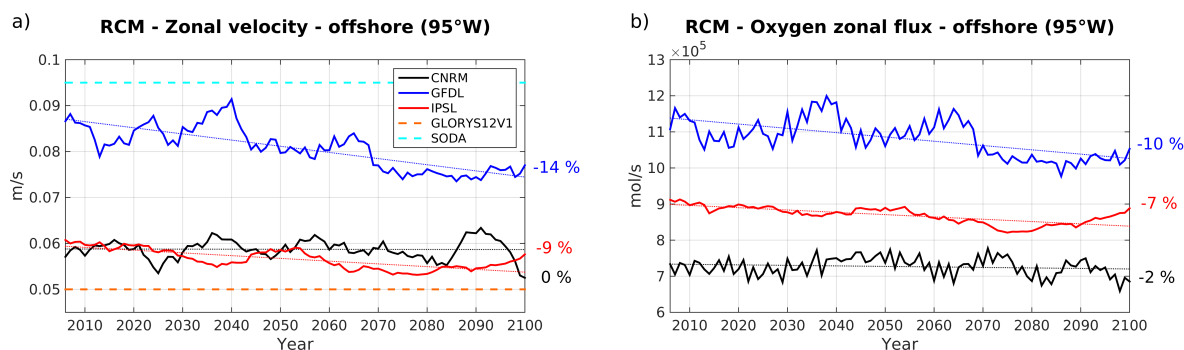


Figure 9: (a) zonal velocity (in m s^{-1}) and (b) oxygen zonal flux (in mol s^{-1}) in the eastern equatorial Pacific at 95°W , averaged between 2N - 10S and 50m - 200m , for the three RCMs (CNRM in black, GFDL in blue, IPSL in red). The timeseries are filtered using a 10-year moving average. Mean values from GLORYS12V1 and SODA reanalyses are marked in (a) by a dashed red line and a dashed light blue line respectively.

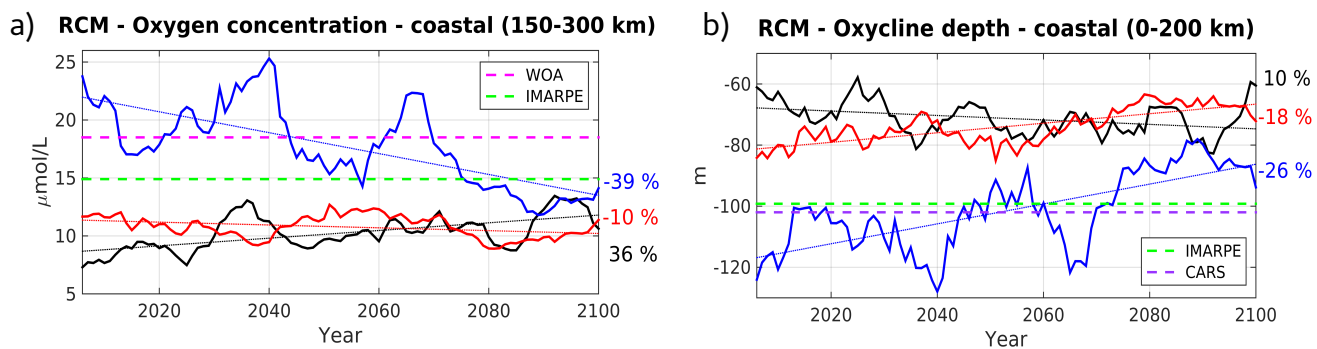


Figure 10: (a) oxygen concentration (in $\mu\text{mol L}^{-1}$) averaged between 100 and 200 meters depth in coastal box located between 150 and 300 km from coast, (b) depth of the oxyclyne ($0.5 \text{ mL L}^{-1} \sim 22 \mu\text{mol L}^{-1}$) isosurface averaged in 200 km-wide coastal box for the three RCMs (CNRM in black, GFDL in blue, IPSL in red). The timeseries are filtered using a 10-year moving average. WOA (dashed magenta line), IMARPE (dashed green line) and CARS (dashed purple line) climatological values are also shown.

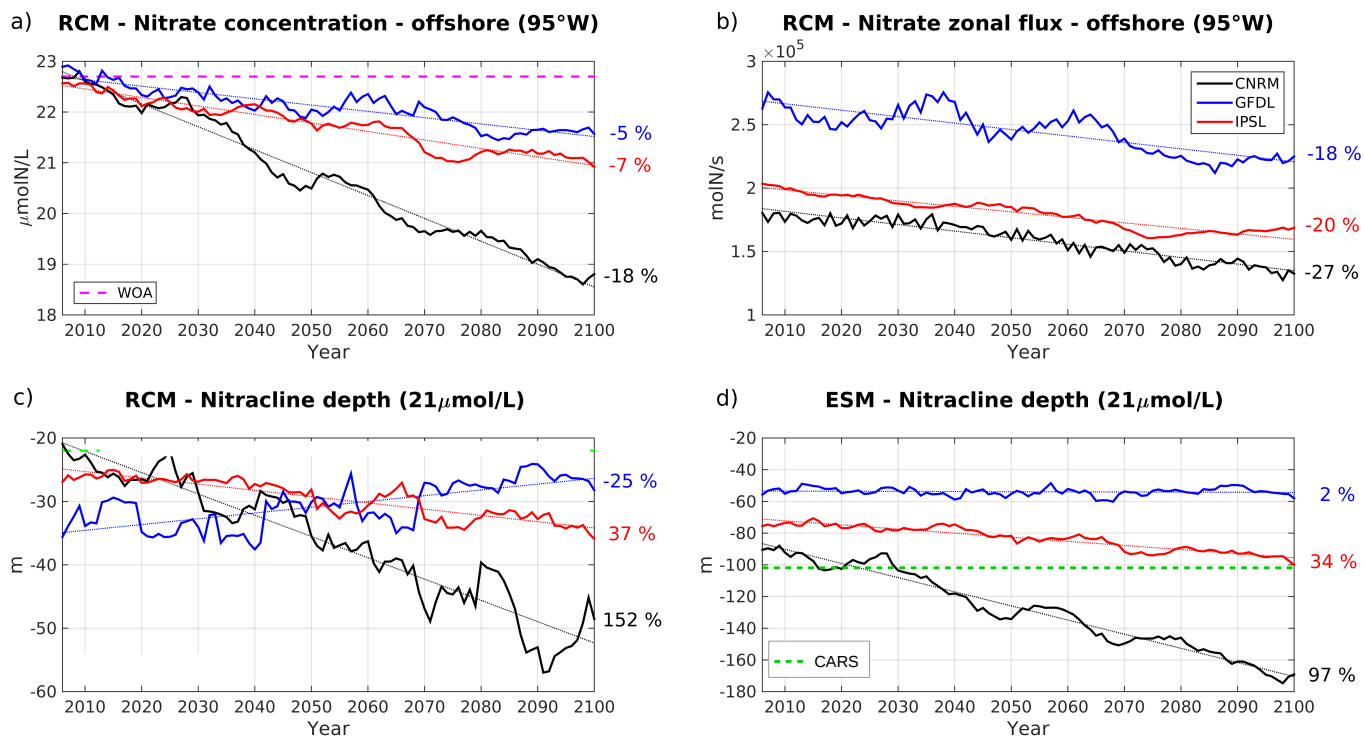


Figure 11: (a) Nitrate concentration (in $\mu\text{mol L}^{-1}$) at 95°W (averaged between 2°N - 10°S , 50-200m depth), (b) nitrate eastward flux (in mol s^{-1}) at 95°W (averaged between 2°N - 10°S , 50-200 m depth) (c) nitracline depth (i.e. depth of the nitrate $21 \mu\text{mol L}^{-1}$ isosurface) averaged in 100km-wide coastal box, for the three RCMs (CNRM in black, GFDL in blue, IPSL in red) and (d) for the ESMs. The timeseries are filtered using a 10-year moving average. WOA (dashed pink line) and CARS (dashed green line) climatological values are shown in (a) and (c).

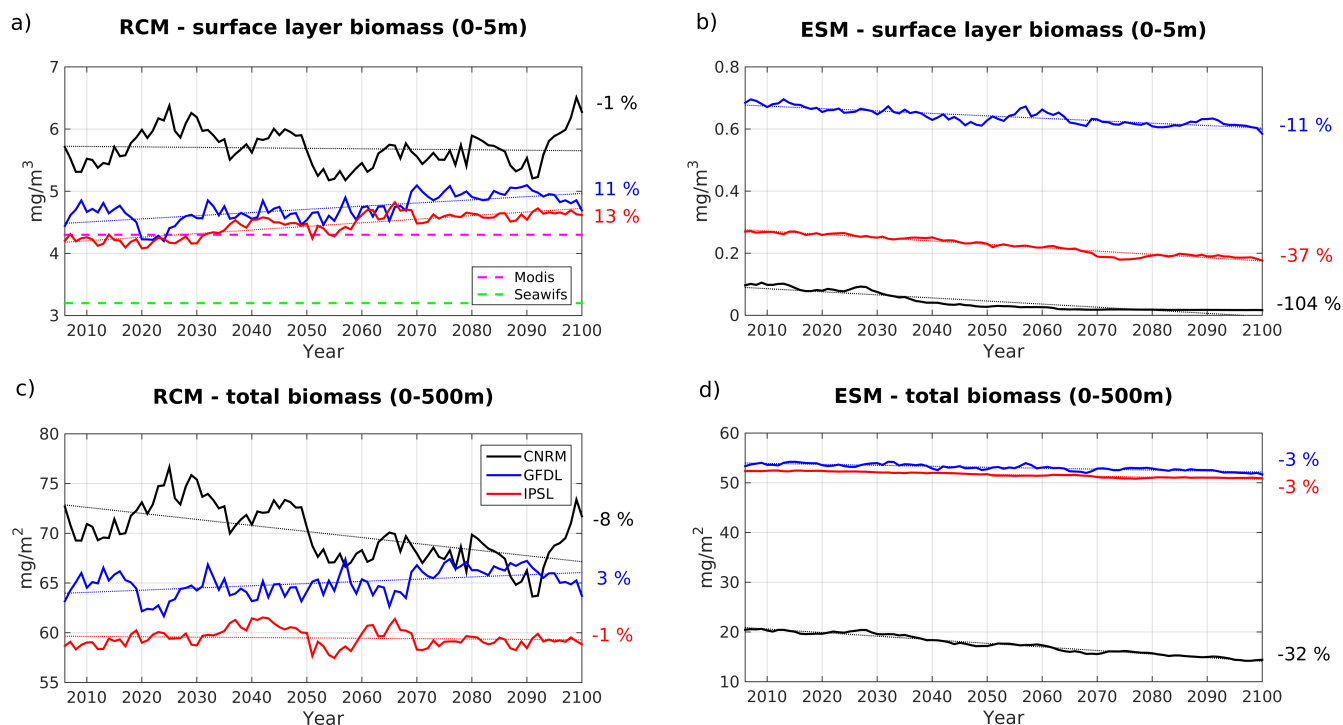


Figure 12: Surface chlorophyll (0-5m, in mgChl m^{-3}) from (a) RCMs and (b) ESMs; depth-averaged chlorophyll concentration (0-50m, in mgChl m^{-2}) from (c) RCMs and (d) ESMs. Color code: CNRM in black, GFDL in blue, IPSL in red. The timeseries are filtered using a 10-year moving average. Thin dotted colored lines indicate the linear trends. All variables are averaged in a coastal box (see Figure 2a). Dashed green and pink lines in (a) mark the mean surface chlorophyll from SeaWiFs (1997-2010) and MODIS (2002-2015) respectively.

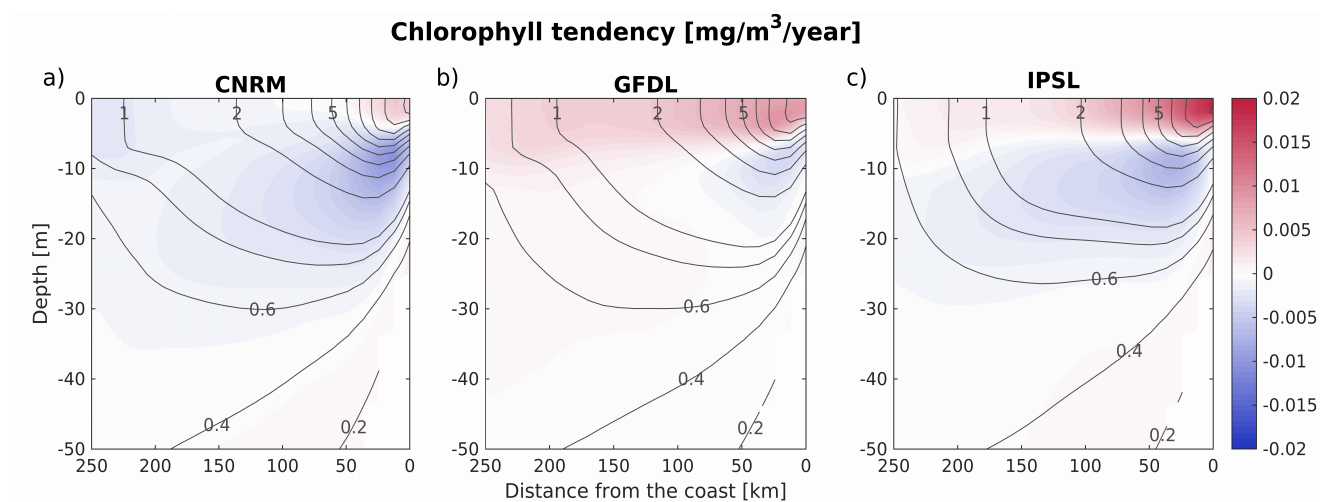


Figure 13: Vertical sections of the RCM chlorophyll linear trends (a-c, in $\text{mg m}^{-3} \text{ year}^{-1}$). The vertical cross-shore section corresponds to an alongshore average of cross-shore sections between 7°S and 13°S.

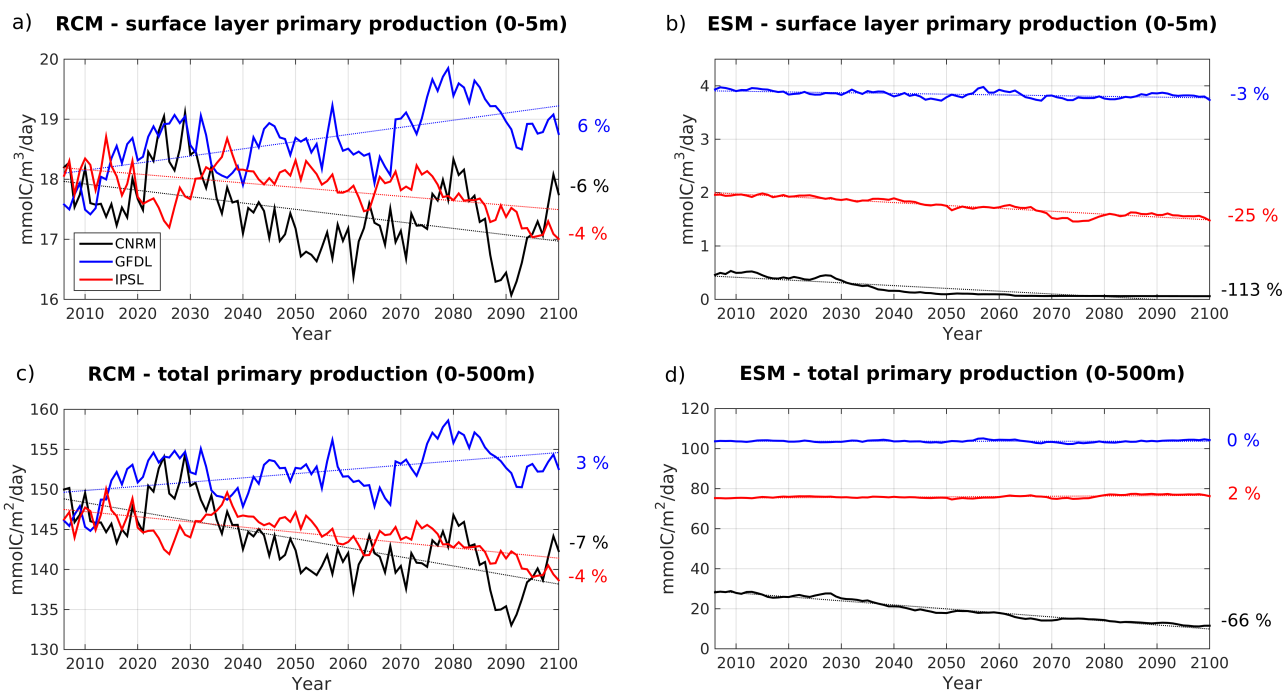
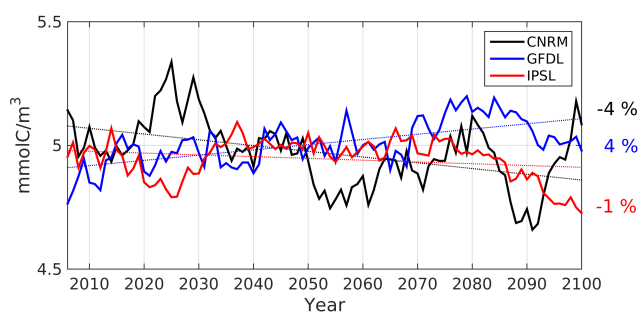


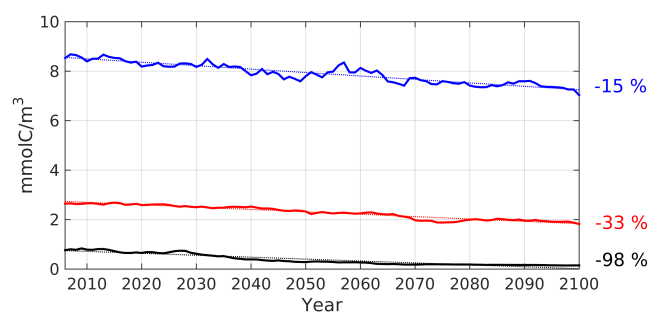
Figure 14: Same as 12 but for primary production (in mmolC/m³/day) for the 0-5m surface layer in (a) and (b) and for the depth-integrated values (in mmolC/m²/day) in (c) and (d).



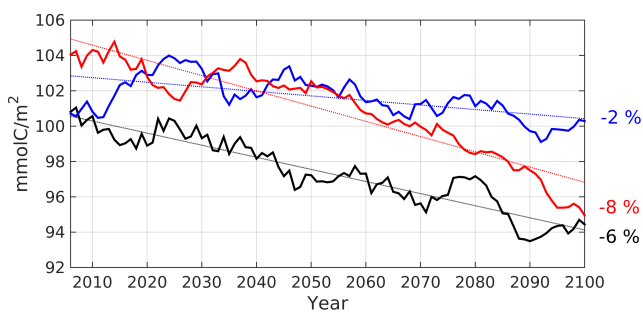
a) RCM - surface layer zooplankton biomass (0-5m)



b) ESM - surface layer zooplankton biomass (0-5m)



c) RCM - total zooplankton biomass (0-500m)



d) ESM - total zooplankton biomass (0-500m)

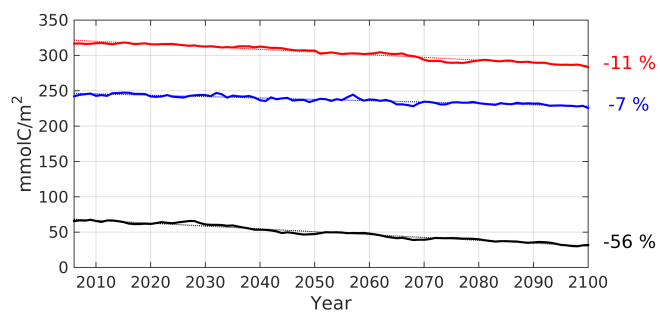


Figure 15: Same as 12 but for zooplankton (in mmolC/m^3) for the 0-5m surface layer in (a) and (b) and for the depth-integrated values (in mmolC/m^2) in (c) and (d).

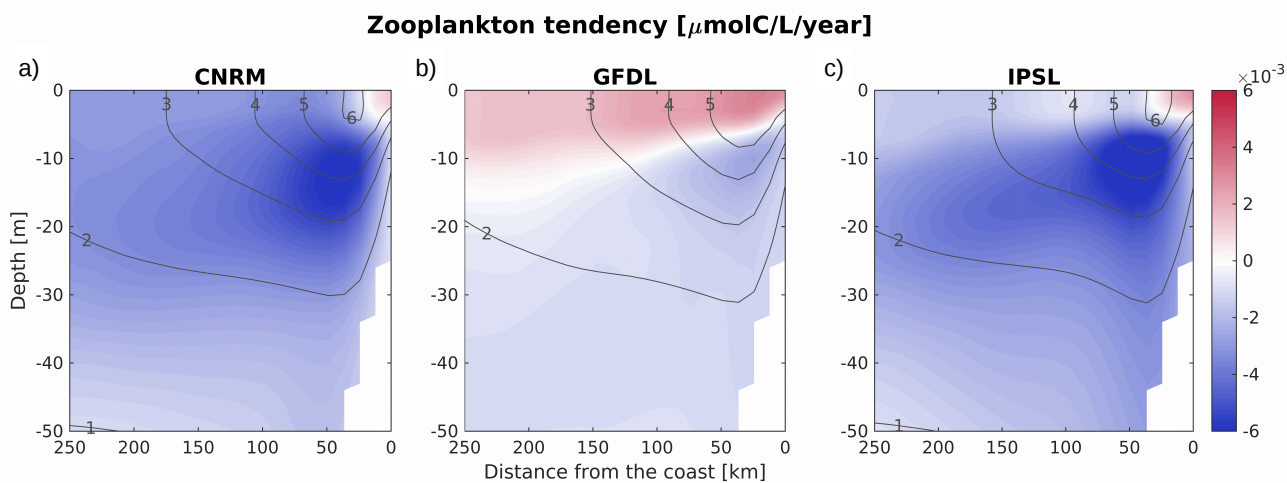


Figure 16: Vertical sections of the RCM zooplankton linear trends (d-f, in $\mu\text{molC L}^{-1} \text{ year}^{-1}$). The vertical cross-shore section corresponds to an alongshore average of cross-shore sections between 7°S and 13°S..

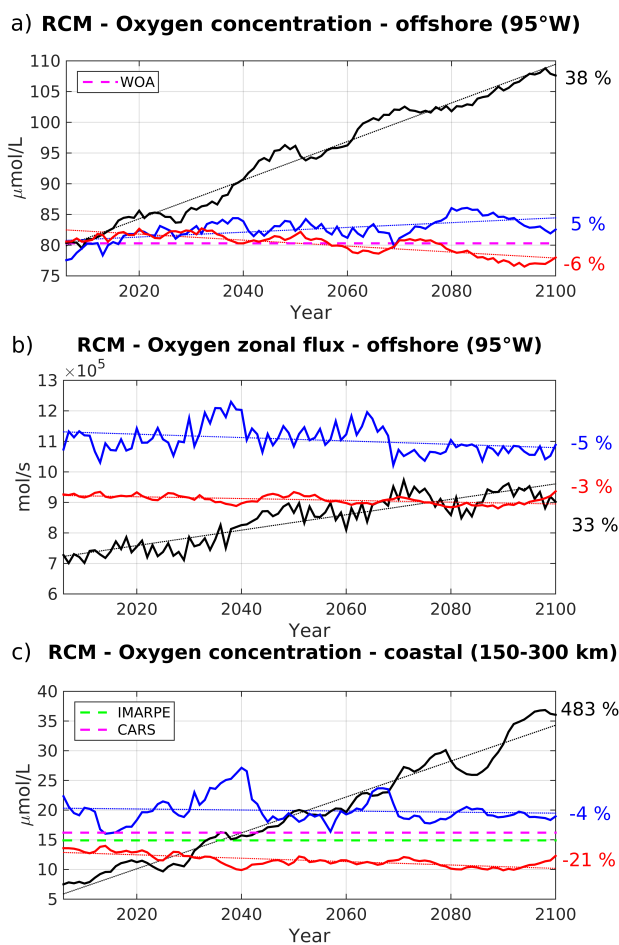


Figure 17: (a) Oxygen content (in $\mu\text{mol L}^{-1}$) averaged in eastern equatorial section (95°W , 2°N - 10°S , 50 - 200 m) in the three ESMS, (b) oxygen flux (in mol L^{-1} , positive eastward) at 95°W , averaged between 2°N - 10°S and 50 m- 200 m (), (c) nearshore subsurface oxygen content (averaged between 100 m and 200 m in coastal box between 150 and 300 km from coast) for the three RCM's (CNRM in black, GFDL in blue, IPSL in red). The timeseries are filtered using a 10-year moving average. WOA (dashed red line), CARS (dashed pink line) and IMARPE (dashed green line) climatological values are also shown.



Earth System Model	Ocean Model	Biogeochemical Model	Horizontal Resolution	Number of vertical levels	References
IPSL-CM5A-MR	NEMOv3.2	PISCES (2 Pg, 2 Zg, N, P, Si, Fe, O ₂)	$\Delta x = 2^\circ$ $\Delta y = 0.5-2^\circ$	31 levels (10 m)	Dufresne et al., Clim Dyn (2013) 40: 2123. https://doi.org/10.1007/s00382-012-1636-1
CNRM-CM5	NEMOv3.2	PISCES (2 Pg, 2 Zg, N, P, Si, Fe, O ₂)	$\Delta x = 1^\circ$ $\Delta y = 0.3-1^\circ$	42 levels (10 m)	Voltaire et al. Clim Dyn (2013) 40: 2091. https://doi.org/10.1007/s00382-011-1259-y
GFDL-ESM2M	MOM4p1	TOPAZ2 (3 Pg, 3 Zg, N, P, Si, Fe, O ₂)	$\Delta x = 1^\circ$ $\Delta y = 0.3-1^\circ$	50 levels (10 m)	Dunne, J. P., et al. 2012. J. Climate, 25, 6646–6665. https://doi.org/10.1175/JCLI-D-12-00150.1

Table 1: Characteristics of the ESMs selected for the regional downscaling.



	Wind stress	Shortwave radiation	Downward longwave radiation	Mixed layer depth	Coastal SST	ESM Coastal SST
CNRM	-11%	-7%	10%	-19%	18%	14%
GFDL	2%	-4%	7%	-16%	10%	9%
IPSL	-9%	0%	10%	-26%	24%	19%
	20°C depth 95°W	20°C depth coast	ESM 20°C depth coast	Velocity along x at 95°W	Offshore flux	Geostrophic flux
CNRM	26%	101%	101%	0%	-23%	-3%
GFDL	5%	12%	21%	-14%	0%	3%
IPSL	71%	207%	126%	-9%	-25%	0%

Table 2: Differences (in %) between 2100 and 2006 (with respect to value in 2006) computed from RCM and ESM linear trends for: wind stress, shortwave radiation, downward longwave radiation, mixed layer depth, coastal SST. Bold font indicates absolute values larger than 50%.



Oxygen						
	Coast 100-200 m	Coast 200-400 m	flux 95°W 50-200 m	Oxycline 22 µmol/L	Oxycline 44 µmol/L	Oxycline ESM
CNRM	36%	51%	-2%	9%	4%	58%
GFDL	-39%	-46%	-10%	-20%	-23%	2%
IPSL	-10%	-13%	-7%	-6%	-7%	-8%
Nitrate						
	Coast 40-100 m	95°W	flux 95°W	vertical flux coast euphotic layer	Nitracline	ESM nitracline
CNRM	-21%	-18%	-27%	-30%	152%	97%
GFDL	-4%	-5%	-18%	-2%	-25%	2%
IPSL	-10%	-7%	-20%	-17%	37%	34%

Table 3: Differences (in %) between 2100 and 2006 (with respect to value in 2006) computed from RCM and ESM linear trends for: nearshore oxygen content, oxygen flux eastward flux, oxycline depth, nearshore nitrate content, nitrate eastward flux, upward nitrate flux into the euphotic layer and ESM nitracline depth. Bold font indicates absolute values larger than 50%.



	Surface Chlorophyll		Total Chlorophyll		Surface Zooplankton		Total Zooplankton	
	RCM	ESM	RCM	ESM	RCM	ESM	RCM	ESM
CNRM	-1%	-104%	-8%	-32%	-4%	-98%	-6%	-56%
GFDL	11%	-11%	3%	-3%	4%	-15%	-2%	-7%
IPSL	13%	-37%	-1%	-3%	-1%	-33%	-8%	-11%

Table 4: Differences (in %) between 2100 and 2006 (with respect to value in 2006) computed from RCM and ESM linear trends for chlorophyll and zooplankton. Total chlorophyll and total zoo indicate depth-integrated values over 0-500m. Bold font indicates absolute values larger than 50%.